NASA TECHNICAL NOTE

NASA TN D-8340 c.1

NASA TN D-8340

PERFORMANCE AND BOUNDARY-LAYER EVALUATION OF A SONIC INLET

James F. Schmidt and Robert S. Ruggeri

Lewis Research Center
Cleveland, Ohio 44135

NATIONAL AERONAUTICS AND SPACE ADMINISTRATION • WASHINGTON, D. C. • NOVEMBER 1976

1. Report No.	2. Government Accession No.	3. Recipient's Catalog No.
NASA TN D-8340		

4. Title and Subtitle
PERFORMANCE AND BOUNDARY-LAYER EVALUATION OF A SONIC INLET

5. Report Date
November 1976

6. Performing Organization Code

7. Author(s)
James F. Schmidt and Robert S. Ruggeri

8. Performing Organization Report No.
E-8579

10. Work Unit No.
505-04

9. Performing Organization Name and Address
Lewis Research Center
National Aeronautics and Space Administration
Cleveland, Ohio 44135

11. Contract or Grant No.

13. Type of Report and Period Covered
Technical Note

12. Sponsoring Agency Name and Address
National Aeronautics and Space Administration
Washington, D.C. 20546

14. Sponsoring Agency Code

15. Supplementary Notes

16. Abstract

Tests were conducted to determine the boundary-layer characteristics and aerodynamic performance of a radial-vane sonic inlet with a length/diameter ratio of 1 for several vane configurations. The sonic inlet was designed with a slight "wavy wall" type of diffuser geometry, which permits operation at high inlet Mach numbers (sufficiently high for good noise suppression) without boundary-layer flow separation and with good total pressure recovery. A new method for evaluating the turbulent boundary layer was developed to separate the boundary layer from the inviscid core flow, which is characterized by a total pressure variation from hub to tip, and to determine the experimental boundary-layer parameters.

17. Key Words (Suggested by Author(s))	18. Distribution Statement
Inlet flow; inlet design; sonic inlet; inlet boundary layers; diffuser design; inlet performance; diffuser boundary layer; turbulent boundary layer; nonequilibrium turbulent boundary layer	Unclassified - unlimited STAR Category 02

19. Security Classif. (of this report)	20. Security Classif. (of this page)	21. No. of Pages	22. Price*
Unclassified	Unclassified	57	$4.50

* For sale by the National Technical Information Service, Springfield, Virginia 22161

CONTENTS

PERFORMANCE AND BOUNDARY-LAYER EVALUATION OF A SONIC INLET

by James F. Schmidt and Robert S. Ruggeri

Lewis Research Center

SUMMARY

Tests were conducted to determine the boundary-layer characteristics and aerodynamic performance of a sonic inlet. The inlet configuration for takeoff used an extended centerbody moved forward to choke the flow in the cowl throat. Further throat-area reductions for the landing inlet configurations were obtained by using radial vanes in the throat region. Data were taken with four sets of blockage vanes consisting of two 35-vane configurations and two 54-vane configurations.

For each of these configurations, experimental total pressure measurements were used to determine the inlet total-pressure recovery, the radial total pressure distribution, and the turbulent-boundary-layer velocity profiles. Surface static pressure measurements were made on the hub and cowl surfaces.

The radial-vane configuration of 35 vanes with tapered thickness (35-tapered-vane configuration) provided the best total pressure recovery over the complete range of normalized average throat Mach number $M_{t,av}$. High average throat Mach numbers ($M_{t,av} > 0.80$), sufficiently large to suppress engine noise radiation through the inlet, were measured for the takeoff (no vane) and landing (35 tapered vane) configurations. The sonic inlet still maintained a high total pressure recovery (greater than 0.975).

The concept of controlling the velocity gradient in the diffuser with a specially designed "wavy wall" type of diffuser geometry not only prevented boundary-layer separation but also tended to minimize the total pressure losses.

A new method for evaluating the turbulent boundary layer was developed to separate the boundary layer from the inviscid core flow, which is characterized by a total pressure variation from hub to tip, and to determine the experimental boundary-layer parameters.

INTRODUCTION

Since a primary source of jet aircraft noise is engine noise, most noise reduction systems are primarily designed to reduce engine noise. Experimental results have convincingly demonstrated that compressor and/or fan noise can be reduced by choking the inlet flow either with inlet vanes or by contracting the cowl walls (refs. 1 to 3). These specially designed inlets, usually referred to as sonic inlets, greatly reduce the engine noise radiating through the inlet by operating at or near the sonic condition (M = 1). However, these high-velocity inlets as compared with conventional inlets) produce reduced inlet total pressure recoveries and increased flow distortion, which could impose a penalty on the aerodynamic performance of the fan and/or compressor. In particular, this reduced aerodynamic performance may significantly reduce the stall margin of a compressor or fan.

Considering the history of proven sonic-inlet noise reduction and the need for good aerodynamic inlet performance, this experimental investigation was conducted to determine the aerodynamic performance and boundary-layer characteristics of a sonic inlet. The inlet configuration for takeoff used an extended centerbody moved forward to choke the flow in the cowl throat. Further throat-area reductions for the inlet landing configurations were obtained by using radial vanes in the throat region. Four flow-blockage vane configurations were used: a 35-tapered-vane configuration, a 35-constant-thickness-vane configuration, a 54-tapered-vane configuration, and a 54-tapered-and-slanted-vane configuration.

The takeoff configuration with the extended centerbody was designed to choke the inlet at the design fan weight flow (33.2 kg/sec). The 35-vane landing configurations were designed to choke the inlet at a weight flow that is 80 percent of the fan design weight flow. Likewise, the 54-vane landing configurations were designed to choke the inlet at a weight flow that is 70 percent of the design flow. Therefore, the 35- and 54-vane configurations represent an operating range for the approach (or landing) configuration.

Increasing the local flow velocity to the near-sonic flow condition and then diffusing to a suitable velocity to achieve good fan performance produce thick wall boundary layers and possible flow separation. Since inlet length and weight must be kept to a minimum, proper adjustment of the inlet to provide sonic or near-sonic flow and then sufficient velocity diffusion without separation represent some of the many compromises required for the design of sonic inlets. Because of the large velocity diffusion produced by the choked flow and the short inlet diffuser, the cowl surface is specially designed with a slight wavy-wall type of geometry to prevent turbulent boundary-layer separation.

Experimental total pressure measurements from passage survey rakes at the fan entrance station were used to determine the inlet total pressure recovery and the radial total pressure distortion. Surface static pressure distributions were measured on both

the hub and cowl surfaces. Strain-gage measurements were also taken on one vane for each vane configuration to determine if a flutter condition occurred. In addition, total pressure measurements from boundary-layer rakes were used to determine the boundary-layer velocity distribution just after the inlet diffuser on the cowl surface and at the fan entrance on both the hub and cowl surfaces. All experimental tests were run without the fan in place over a range of weight flows from a low value to the maximum weight flow.

A new method for evaluating the turbulent boundary layer was developed to separate the boundary layer from the inviscid core flow, which is characterized by a total pressure variation from hub to tip, and to determine the experimental boundary-layer parameters.

APPARATUS AND PROCEDURE

The experimental facility used in this investigation, except for the installation of the sonic inlet (fig. 1), is the same as the compressor test facility described in reference 4. Atmospheric air enters the test facility from an inlet on the roof of the building; flows through the various valves, piping, plenum, and the test section; and then exhausts to a low-pressure (67.6-pascal (20-in.-Hg) vacuum) exhaust system.

Inlet Design

The sonic-inlet configuration showing the extended centerbody and the location of the radial vanes is illustrated in figure 2. The cowl portion of the inlet consists of an entering flight-lip type of geometry converging to the throat region with a following diverging diffuser section emptying into an existing straight section. The straight section houses the five slanted support struts, which produced a 2 percent blockage in the flow. These slanted support struts have an axial chord length of 5.41 centimeters and are located just after the diffuser section (fig. 2). The hub centerbody, which was an existing part, is composed of a spinner type of nose design proceeding to the throat section with a following (slight linear variation) section that continues to the end of the diffuser. Thus, this diffuser design consisted of contouring the cowl surface from the throat to the diffuser outlet (a Mach number diffusion of from 1.0 to 0.34 in a distance of 27.60 cm) such that boundary-layer separation was avoided.

Two flow-analysis codes were applied. The first was an inviscid-flow calculation code, and the second a turbulent-boundary-layer calculation code. The inviscid-flow code requires that a geometry be specified, and the boundary-layer flow code requires

that a pressure (velocity) distribution be specified. Thus, the design procedure becomes an indirect and iterative process. The diffuser design guideline used to avoid boundary-layer separation was that the boundary-layer form factor H should always be less than 2.2. The turbulent-boundary-layer calculation method (ref. 5) was used to determine H and other boundary-layer parameters. The boundary layer, which starts near the stagnation point, was assumed to be turbulent over the entire length of the inlet. The form factor H was found to be insensitive to the initially assumed value for the turbulent-boundary-layer thickness near the stagnation point. An inviscid-flow calculation method, from an in-house compressor aerodynamic flow design program that considers streamline-curvature and flow-blockage effects, was used to determine the free-stream Mach number distribution for a given or assumed diffuser geometry. This free-stream Mach number distribution was then used as input to the boundary-layer program.

The first step in designing the diffuser was to determine the general free-stream Mach number distribution that would prevent boundary-layer separation but still provide the required velocity diffusion. Then the cowl geometry was modified until the inviscid-flow calculation produced the desired Mach number distribution along the cowl surface, including the boundary-layer displacement effect on the flow. The boundary-layer form factor was maintained under a limiting value of 2.2 by judiciously varying the rate of velocity diffusion. Figure 3 shows the slight wavy-wall type of geometry that evolved from calculations based on this design philosophy. This wavy-wall type of geometry occurred almost immediately downstream of the vanes on the cowl surface. First, it was necessary to take the maximum velocity diffusion as soon as possible after the throat while the turbulent boundary layer was still quite small. Then, before the form factor H became too large (an indication of separation), the slight wavy-wall type of geometry was encountered, which reversed the direction of H (fig. 3). For the remaining portion of the diffuser only a small amount of velocity diffusion was required, which resulted in good control over the form factor and thereby the turbulent boundary layer. Figure 3 also shows the resulting change in the free-stream Mach number after the throat that is required to reverse the direction of H. Surface coordinates of the cowl and hub centerbody are given in figure 2.

The sonic inlet with the radial vanes in place as shown in figure 2 is the approach (or landing) inlet configuration. The takeoff inlet configuration consists of this same inlet but with the radial vanes removed or retracted. The four landing vane configurations were a 35-tapered-vane configuration, a 35-constant-thickness-vane configuration, a 54-tapered-vane configuration, and a 54-tapered-and-slanted-vane configuration.

To obtain a true comparison of the tapered- and constant-thickness vanes, the tapered-thickness vane was designed with the same integrated, flow-blockage, cross-sectional area as the constant-thickness vane. The surface coordinates for the

constant-thickness vanes, which have a $t_{v,max}/c$ of 10 percent, are given in figure 4. In figure 5, the surface coordinates are given for the tapered-thickness vanes, which have $t_{v,max}/c$ of 6 percent at the hub to 14 percent at the tip. These vanes are tapered with the thinnest section at the hub in order to produce the smallest possible throat flow blockage in a region where the cross-sectional flow area is the smallest. The slanted vanes were also designed with a tapered thickness and are slanted at approximately 28° (fig. 6). The reason for testing a slanted vane configuration is that some unpublished results have suggested that improved aerodynamic performance can be obtained with slanted blades. An angle view of a tapered vane and a vane with constant thickness is shown in figure 7.

The 35-vane configuration was designed to choke the inlet with a weight flow that is 80 percent of the fan design weight flow (32.2 kg/sec) for the two-stage fan with a tip speed of 426 meters per second. Similarly, the 54-vane configuration was designed to choke the inlet at a weight flow that is 70 percent of the design weight flow. The 35- and 54-vane configurations produce throat-area flow reductions of 19.23 and 29.67 percent, respectively. The 35-vane configuration installed in the sonic inlet is shown in figure 8. Likewise, figures 9 and 10 show the 54-vane configuration with tapered vanes and the 54-vane configuration with tapered and slanted vanes, respectively, installed in the sonic inlet. For each configuration the vanes were pin-connected at the hub and bolted to a ring spacer at the cowl.

Instrumentation

Axial locations of the survey rake instrumentation as well as the static pressure taps are shown in figure 11, and their circumferential locations are shown in figure 12. In the plenum chamber, two pressure taps and two thermocouples were used to measure the total pressure and total temperature. A calibrated orifice plate upstream of the plenum and the test section was used to measure the weight flow.

The detailed dimensions of the five total pressure rakes at the fan entrance are given in figure 12. Each total pressure rake had six tubes that were designed to be located at the corresponding center of six equal cross-sectional areas, the sum of which equals the total flow-passage area. This particular orientation of the total pressure tubes made it particularly simple to calculate the area-weighted average of all total pressure rake measurements. The detailed dimensions of the three total pressure boundary-layer rakes are given in figure 13, which shows one rake on the cowl surface and another rake on the hub surface at the fan entrance axial location. The remaining boundary-layer rake is located on the cowl surface just a short distance from the diffuser section, as already indicated in figure 11.

The static and total pressure measurements were made with a strain-gage type of transducer. A representative vane for each vane configuration was strain gaged in order to observe vane stresses and to determine if a flutter problem existed, especially near the choking weight flow. All data were automatically and centrally recorded on magnetic tape.

Test Procedure

The sonic inlet was operated over a wide range of average throat Mach numbers by accurately regulating the air weight flow with the exhaust valve. After the exhaust valve was set, the automatic, on-line, data reduction program was used to determine the average throat Mach number and the total pressure recovery as well as the exact measured experimental weight flow. Then, if necessary, a fine vernier change to the exhaust valve setting could be performed for a more accurate desired weight flow. This test procedure became particularly useful in obtaining the desired flow condition near and at the choking weight flow, because a relatively small change in weight flow now produced a significant change in the total pressure recovery. After the desired flow condition was obtained, the data were automatically and centrally recorded on magnetic tape. Also, the stresses on the instrumented vanes were checked at each flow condition.

Data Reduction

All measured data were converted to SI units and corrected to standard conditions.

Calculation of flow properties and aerodynamic performance. - One-dimensional flow equations along with the measured data were used to calculate the velocity, Mach number, temperature, and density along the hub and cowl surfaces. The average throat Mach number $M_{t,av}$ was calculated from the following one-dimensional flow equation (ref. 6):

$$\frac{W_m}{A_{eff}} = \left(\frac{\gamma}{RT_0}\right)^{1/2} \left[\frac{P_0 M_{t,av}}{\left(1 + \frac{\gamma - 1}{2} M_{t,av}^2\right)^{(\gamma+1)/2(\gamma-1)}}\right] \tag{1}$$

(See the appendix for definitions of all symbols.) The effective throat area A_{eff} is

$$A_{eff} = A_{tt} - A_{vb} \tag{2}$$

where the total throat area A_{tt} without vanes is

$$A_{tt} = \pi\left[\left(r_c\right)^2 - \left(r_b\right)^2\right] \tag{3}$$

The vane blockage area A_{vb} at the geometric throat is

$$A_{vb} = (n_v)(t_v)(r_c - r_h) \tag{4}$$

The average throat Mach number is easily obtained from equation (1) with an iterative procedure using the known values of measured weight flow, total plenum pressure and temperature, and effective throat area. As used in reference 3, the normalized average throat Mach number, which is useful for comparing different inlet configurations, is defined as

$$M_{t,n} = \frac{M_{t,av}}{\left(M_{t,av}\right)_{max}} \tag{5}$$

where $\left(M_{t,av}\right)_{max}$ is the maximum value of the average throat Mach number, which occurs at the fully choked flow condition.

Total pressure rake measurements at the fan entrance are used to calculate the total pressure recovery

$$R_c = \frac{P_{aa}}{P_0} \tag{6}$$

where P_{aa}, the area-weighted average total pressure, is

$$P_{aa} = \frac{\sum_{i=1}^{n} A_i P_i}{\sum_{i=1}^{n} A_i} \tag{7}$$

Boundary-layer evaluation. - At higher average throat Mach numbers ($M_{t,av} \geq 0.80$), large radial total pressure distortion from hub to cowl was measured at the fan entrance. This large total pressure distortion reflects not only the total pressure loss due to the turbulent boundary layer, but also a large loss due to the flow disturbance of the choking vanes upstream in the throat region. Therefore, it becomes a very difficult problem to separate the total pressure boundary-layer distribution from the rotational, inviscid, total pressure distribution. This problem is further complicated by the fact that not only is the usual boundary-layer thickness unknown, but also the free-stream (edge of the boundary layer) velocity is unknown. To calculate the standard boundary-layer parameters from the measured boundary-layer data, it is necessary to find some means of calculating or approximating the boundary-layer edge velocity as well as separating the total pressure boundary-layer distribution from the inviscid total pressure distribution. By using an approximate engineering approach, the following turbulent-boundary-layer data reduction program was developed. It is roughly based on the concept of "matched asymptotic expansions" as described by Van Dyke (ref. 7). An iteration procedure was used for establishing U_e that incorporated this general concept of matched asymptotic expansions. The boundary-layer calculation is referred as "the method of construction of the boundary layer from rotational core flows."

From Van Dyke's original concept (ref. 7) and as suggested for internal flows by Mellor and Wood (ref. 8), the measured velocity across an annular passage with total pressure variation is given by

$$U_m = U_b + U_{inv} - U_e \tag{8}$$

where U_m is the overall measured velocity profile, U_b is the inner expansion or boundary-layer velocity profile, U_{inv} is the outer expansion or inviscid velocity profile, and U_e is the common asymptote or boundary-layer edge velocity. Figure 14 graphically describes this method of construction of the boundary layer from rotational core flows applied to the data for one representative sonic-inlet flow condition.

The measured velocity profile U_m was determined from the standard compressible flow relations by using the measured total and static pressures and the measured plenum temperature. Since the boundary-layer total pressure measurements did not extend far enough into the inviscid core region, an average of the five total pressure rake measurements at each radial position was used to determine the measured velocity profile in the central core region of the channel (figs. 15 and 16). These total pressure rake measurements at the fan entrance axial location were assumed to be valid for station 19 (just after the end of the diffuser). The loss of total pressure due to the support struts was assumed to be small such that the radial total pressure distribution in the core flow at station 19 is essentially the same as at the fan entrance. The inviscid

velocity profile U_{inv} was only known far from the cowl or hub surface (equal to U_m in the core of the annular passage) and outside the boundary layer. However, with an initial value of U_e, the outer values of the inviscid velocity profile were curve fit with a quadratic equation to the wall value (U_e). With distributions of U_m, U_{inv}, and an initially assumed value for U_e, the boundary-layer velocity profile U_b was calculated from equation (8).

As previously suggested, some means of calculating or approximating the boundary-layer edge velocity U_e is needed along with equation (8) to determine the experimental boundary-layer profile U_b. The general calculational procedure consists of an iteration for U_e until the correct boundary-layer edge velocity is obtained. First, an initial value of U_e is assumed and the inviscid velocity profile U_{inv} is obtained by curve fitting the outer core velocities to the wall value U_e. Second, the boundary-layer profile U_b is calculated from equation (8) with the calculated U_{inv} and the assumed U_e. Then, the skin friction coefficient C_f can be approximated by using the first two data points in a "law of the wall" model with U_e. The momentum thickness θ, the displacement thickness δ^*, and the form factor H can be calculated by using the calculated U_b and the assumed U_e. Finally, a new U_e can be obtained from Ludwieg and Tillman's empirical relation (ref. 10) for the skin friction coefficient C_f by using the previously calculated θ, H, and C_f. Thereby, this process is repeated until the correct iterated value of U_e is calculated and hence the proper boundary-layer profile U_b is automatically obtained.

A detailed account of this general iteration procedure for U_e is given by the following formulation of equations. By using the assumed U_e and the first two data points nearest the wall, the experimental skin friction coefficient can be calculated according to the law-of-the-wall model (ref. 9)

$$U^+ = \frac{U_b}{U_e} \frac{1}{\left(\frac{C_f}{2}\frac{t_{aw}}{t_e}\right)^{1/2}} = 5.75 \log_{10} Y^+ + 5.5 \tag{9}$$

where the dimensionless wall distance parameter Y^+ can be expressed as

$$Y^+ = \frac{\rho_e U_e Y}{\mu_{aw}} \left(\frac{C_f}{2}\right)^{1/2} \left(\frac{t_e}{t_{aw}}\right)^{1/2} \tag{10}$$

where Y is the boundary-layer distance, t_{aw} is the adiabatic wall temperature, t_e is

the temperature at the edge of the boundary layer, ρ_e is the density at the edge of the boundary layer, and μ_{aw} is the dynamic viscosity based on the adiabatic wall temperature.

After rearranging equation (9), the skin friction coefficient is calculated from the following equation:

$$\left(\frac{C_f}{2}\right)^{1/2} = \frac{\left(\frac{U_b}{U_e}\right)\left(\frac{t_e}{t_{aw}}\right)^{1/2}}{5.75 \log_{10} Y^+ + 5.5} \tag{11}$$

Equation (11) is applied at the first two data points and averaged to get $C_f/2$. Initially, a value for $C_f/2$ is assumed in equation (9), and the correct value of $C_f/2$ is found by iteration of equations (9) and (11).

Since the Mach number was low in the straight annular section where the boundary-layer rakes were located, the flow was considered to be incompressible. The assumed U_e and the calculated boundary-layer velocity profile U_b were used to calculate the following incompressible momentum and displacement thicknesses:

Momentum thickness:

$$\theta = \int_0^{Y_{inv}} \frac{U_b}{U_e}\left(1 - \frac{U_b}{U_e}\right) dY \tag{12}$$

Displacement thickness:

$$\delta^* = \int_0^{Y_{inv}} \left(1 - \frac{U_b}{U_e}\right) dY \tag{13}$$

where Y_{inv} is the distance from the wall associated with the maximum measured core velocity.

The form factor H is defined as

$$H = \frac{\delta^*}{\theta} \tag{14}$$

The Ludweig-Tillman empirical relation for the skin friction coefficient from reference 10 is

$$\frac{C_f}{2} = 0.123\left(e^{-1.561H}\right)\left[\frac{\mu_{ref}}{\rho_0 U_e \theta}\left(1 + \frac{\gamma - 1}{2} M_e^2\right)^{1/(\gamma-1)}\right]^{0.268}\left(\frac{t_e}{t_{ref}}\right) \tag{15}$$

where ρ_0 is the density based on total conditions, M_e is the Mach number at the edge of the boundary layer, μ_{ref} is the dynamic viscosity based on reference temperature, and the reference temperature (ref. 11) is given by

$$t_{ref} = t_e\left[1 + 0.72(Pr)^{1/3}\frac{\gamma - 1}{2} M_e^2\right] \tag{16}$$

where the Prandtl number Pr is assumed to be 0.71.

After solving for U_e in equation (15), the new velocity at the edge of the boundary layer becomes

$$U_e = \left[\left(\frac{0.123}{\frac{C_f}{2} e^{1.561H}}\right)\left(\frac{t_e}{t_{ref}}\right)\right]^{1/0.268}\left[\frac{\mu_{ref}\left(1 + \frac{\gamma - 1}{2} M_e^2\right)^{1/(\gamma-1)}}{\rho_0 \theta}\right] \tag{17}$$

where $C_f/2$, θ, H, and other terms in equation (17) have already been calculated for the previously assumed value of U_e.

After each new U_e is determined, a new total pressure P_e can be calculated, by using the new U_e and the measured static pressure, from an iteration of the following equations:

$$M_e = \frac{U_e}{(\gamma R t_e)^{1/2}} \tag{18}$$

$$P_e = p_w\left[\left(1 + \frac{\gamma - 1}{2} M_e^2\right)^{\gamma/(\gamma-1)}\right] \tag{19}$$

$$t_e = T_0\left(\frac{p_w}{P_e}\right)^{(\gamma-1)/\gamma} \tag{20}$$

The general iteration procedure for U_e is summarized by the following steps:

(1) The measured velocity profile U_m is determined from the standard flow relations by using the measured static and total pressures and the measured plenum temperature.

(2) The inviscid velocity profile U_{inv} is obtained by curve fitting the outer core velocities to the initially assumed wall value U_e.

(3) The boundary-layer profile U_b is calculated from equation (8) by using the calculated U_{inv} and present value of U_e.

(4) With U_e and the first two data points for U_b and Y known, equations (9) to (11) are solved for C_f.

(5) By using U_e and U_b, the boundary-layer quantities δ^*, θ, and H are calculated from equations (12) to (14).

(6) With the calculated H, θ, and C_f, equation (17) is solved for a new U_e.

(7) By using the new U_e and equations (18) to (20), a new total pressure P_e is calculated.

(8) With the new U_e and P_e, steps 2 to 7 are repeated until the final iterated U_e is obtained.

RESULTS AND DISCUSSION

The aerodynamic performance of the sonic inlet (table I includes representative data points) with the various vane configurations is discussed in terms of the total pressure recovery, the radial distribution of total pressure at the fan entrance, and the Mach number distributions along the hub and cowl surfaces. The total pressure recovery is presented as a function of the average throat Mach number, which approaches a maximum value for each vane configuration as the inlet reaches a choked flow condition. In addition, the aerodynamic performance is discussed in terms of the measured wall boundary-layer characteristics, which can have a major influence on the aerodynamic performance as the choked condition is approached. The total pressure boundary-layer measurements were not used in calculating the total pressure recovery. Since the tubes of the total pressure rakes across the annulus are designed to be located on the basis of equal cross-sectional areas (fig. 12), inclusion of the boundary-layer measurements for the 35-tapered-vane configuration resulted in a negligible effect on the total pressure recovery (<0.5 percent).

Although this experimental study is primarily directed at aerodynamic performance, some estimate of the average throat Mach number at which a sonic inlet will significantly reduce the engine noise radiated out the inlet is desirable. For this estimate, the noise results of reference 12 were used. The sonic-inlet noise tests of reference 12 disclose that a significant noise reduction of 10 decibels or greater occurs for $M_{t, av} \approx 0.80$. As $M_{t, av}$ is increased above 0.80, the noise reductions also increase rapidly.

Aerodynamic Performance

In addition to the aerodynamic performance of the sonic inlet for the takoff (no vane) configuration, the experimental results for the two 35-vane landing configurations and the two 54-vane landing configurations are also presented and discussed.

Before a fair comparison of experimental results for different radial-vane inlet configurations can be made, a common basis of comparison must be established. Total pressure recovery, the primary measure of aerodynamic performance, is presented in figure 17 as a function of the average throat Mach number for the sonic inlet with all the radial-vane configurations studied. This average throat Mach number approached a maximum value as the choking weight flow was attained (fig. 17). This implies that the sonic inlet with its particular vane configuration has reached a choked flow condition. Figure 17 also shows that for each particular vane configuration the sonic-inlet flow choked at a different value of the average throat Mach number, because of the effective area blockage of the vanes. Because of this significantly different value of the average throat Mach number at the choked condition for each vane configuration, the total pressure recovery is also presented as a function of the normalized throat Mach number (fig. 18). The normalized throat Mach number is defined as the ratio of the average throat Mach number to the average throat Mach number at the choked condition (ref. 3). Thereby, the normalized throat Mach number goes to unity at the choked condition for all sonic inlets, and different sonic inlets and/or vane configurations can now be compared.

The sonic inlet with the 35-tapered-vane configuration (fig. 18) gave the best total pressure recovery of all vane configurations over the complete range of the normalized throat Mach number. This result is understandably evident from figure 19, which shows that the 35-tapered-vane configuration also produced the most uniform and best total pressure distribution from hub to cowl with the ensuing lowest end-wall, boundary-layer losses. Since the tapered vane was designed to have the same cross-sectional, flow-blockage area as the constant-thickness vane, the 35-tapered-vane configuration and the 35-constant-thickness-vane configuration can be directly compared. The total pressure recovery for the 35-constant-thickness-vane configuration was substantially less than

the total pressure recovery for the 35-tapered-vane configuration (fig. 18). In fact, the total pressure recovery for the 35-constant-thickness-vane configuration was about the same as that for the 54-tapered-vane configuration, even though the 54 vanes yield a much larger throat-area blockage. The reason for this poor aerodynamic performance of the 35-constant-thickness-vane configuration can be traced to the very large total pressure distortion and the probable boundary-layer separation in the hub region (fig. 19). This large total pressure distortion in the hub region results from the larger throat-area blockage in this region for the constant-thickness vanes as compared with the tapered vanes. Also, from the strain-gage measurements the constant-thickness vane was the only vane design that experienced a flutter problem, and this occurred for $M_{t,av} > 0.85$.

Also of special interest in figure 18, the sonic inlet with the 54-tapered-and-slanted-28^{o}-vane configuration produced a higher total pressure recovery than the 54-tapered-vane configuration. Consistent with this result, figure 19 shows a slightly better total pressure distribution (lower distortion) mostly in the hub region for the 54-tapered-and-slanted-28^{o}-vane configuration.

This improved total pressure distribution in the hub region for the 54-tapered-and-slanted-28^{o}-vane configuration may result from the greatly reduced local flow Mach number in this region. Static pressure measurements on the annulus walls revealed that, along the cowl surface, the Mach number distributions were similar but that, along the hub surface, the peak flow Mach number distribution (throat region) for the slanted vanes was significantly lower (about half) than that for the radial vanes. These results disclose that some aerodynamic benefits from slanting the vanes were realized (at least for the angle at which the vanes were slanted). Unfortunately, the measured data were not sufficiently detailed to allow a complete explanation of the flows with slanted vanes.

After having compared the aerodynamic performance of the various radial-vane configurations in the present sonic inlet, it is of interest to compare the present results with previous sonic-inlet tests. Therefore, the total pressure recovery of the present sonic inlet was compared with the total pressure recovery of one of the sonic inlets selected from reference 3. The sonic inlet selected from reference 3 had a radial configuration of 36 tapered vanes and a length/diameter ratio similar to that of the present sonic inlet. However, the vanes of the reference 3 configuration were much thicker than the vanes used in the present inlet. In fact, the 36-vane configuration of reference 3 produced a cross-sectional, throat-area reduction of 27 percent. And this is almost comparable to the present 54-tapered-vane-configuration, throat-area reduction of 29.67 percent. In addition, the total pressure was measured nearer to the cowl surface but farther away from the hub surface for the present inlet than for the reference 3 inlet.

Figure 18 shows that the present sonic inlet with the 54-tapered-vane configuration has a higher overall total pressure recovery than the sonic inlet with the 36-vane configuration of reference 3. Since the sonic inlet with the 35-tapered-vane configuration produced the best overall total pressure recovery of all vane configurations, the general aerodynamic performance of this sonic-inlet (landing) vane configuration as well as the takeoff (no vane) configuration are discussed in more detail.

Takeoff (no vane) configuration. - First, for the takeoff (no vane) configuration, figure 17 shows that the total pressure recovery decreased slightly with an increasing average throat Mach number $M_{t,av}$ to a value of 0.988 and then decreased rather abruptly.

The apparent reason for this abrupt decrease in the total pressure recovery is as follows: For an average throat Mach number of 0.917, figure 20, which gives the distribution of the cowl surface Mach number M_c, indicates a peak value (1.07) of M_c just a short distance (2 cm) from the geometric throat. Also of interest in figure 20 is the distribution of M_c, which peaked at two axial locations along the cowl for an average throat Mach number of 0.947. The first peak value of M_c (1.1) occurred slightly upstream of the geometric throat, and the second peak (approx 1.24) occurred 3.5 centimeters downstream of the geometric throat. For the hub surface, figure 21 shows that a single peak value (1.14) of the hub surface Mach number M_h occurred 1.25 centimeters downstream of the geometric throat for an $M_{t,av}$ of 0.947. Although the double-peaked surface Mach number distribution on the cowl surface and also the large peak Mach numbers ($M > 1.0$) on both the hub and cowl surfaces may suggest a shock-wave occurrence, the lack of a sharp discontinuity in the surface static pressure measurements (hence, M_c and M_h) suggests that strong normal shocks were not present.

Especially note from figures 20 and 21 that not only did a greater peak value of the surface Mach number occur on the cowl surface, but also a steeper Mach number gradient was impressed upon the cowl surface as compared with the hub surface. Therefore, the rate as well as the amount of velocity diffusion was much greater on the cowl surface, especially at larger average throat Mach numbers. Now, by comparing the total pressure distributions from hub to cowl for $M_{t,av}$ of 0.917 and 0.947 in figure 15, we see that a much larger total pressure loss occurred in the cowl region and predominately for $M_{t,av}$ of 0.947. Hence, in the concluded absence of any significant normal shock waves, the abrupt decrease of the total pressure recovery for $M_{t,av} > 0.917$ is attributed to the large boundary-layer losses on the cowl surface that result from the large velocity diffusion along the cowl surface.

An example of this extreme change in the turbulent boundary layer on the cowl surface is shown by the rapid increase in the experimental momentum and displacement thicknesses for $M_{t,av} > 0.917$ in figure 22. On the hub surface, figure 23 shows a negligible change in the experimental momentum and displacement thicknesses for

$M_{t,av} > 0.917$. The magnitude of the boundary-layer thicknesses in figure 23 also indicates a very small boundary-layer loss on the hub surface.

A very important observation for the takeoff (no vane) configuration is that the peak throat surface Mach numbers of 1.07 on the cowl surface and 0.99 on the hub surface for $M_{t,av}$ of 0.917 should be sufficiently high to suppress engine noise radiation through the inlet while the sonic inlet still maintains a high total pressure recovery of 0.988. Significant engine noise reductions should be realized with this level of $M_{t,av}$.

Landing (35 tapered vane) configuration. - Similar to the takeoff (no vane) configuration, the total pressure recovery for the 35-tapered-vane landing configuration decreased moderately with increasing $M_{t,av}$ to a value of 0.970 at an $M_{t,av}$ of 0.869. Then the total pressure recovery decreased abruptly (fig. 17).

This abrupt decrease in the total pressure recovery is explained as follows: Figures 24 and 25, which present the experimental Mach number distributions along the hub and cowl surfaces, show not only very large maximum surface Mach numbers but also steep Mach number gradients for both the hub and cowl surfaces in the throat region at $M_{t,av} > 0.800$. In fact, the maximum surface Mach number and the steep Mach number gradients were even greater on the hub surface than on the cowl surface for $M_{t,av} > 0.800$. By comparing figures 24 and 25 with figures 20 and 21, we see that the surface Mach number gradients were much steeper for the landing (35 tapered vane) configuration than for the takeoff (no vane) configuration, especially on the hub surface. The presence of the choking vanes produced the large surface Mach number gradients on both the hub and cowl surfaces as well as an additional, total pressure, vane wake loss. However, the lack of a distinct sharp discontinuity in the surface static pressure measurements for the 35-tapered-vane configuration implies that large normal shock waves did not occur, even though the maximum surface Mach numbers were greater than 1.0.

By comparing the total pressure distributions from hub to cowl for $M_{t,av}$ of 0.843 to 0.899 in figure 16, we see that large total pressure losses for the landing configuration occurred in both the hub and cowl regions. An appreciable part of this total pressure loss may be due to the wake loss of the choking vanes. But the major reason for the abrupt decrease of the total pressure recovery for $M_{t,av} > 0.869$ is the combined interaction of these wake losses with the large boundary-layer losses on the hub and cowl surfaces. This rapid boundary-layer growth on the cowl surface is shown in figure 26 by the strong increase in the experimental momentum and displacement thickness for $M_{t,av} > 0.869$. On the hub surface, figure 23 also shows this large increase in the experimental momentum and displacement thicknesses for $M_{t,av} > 0.869$.

Based on noise benefit guidelines, an important observation for the 35-tapered-vane landing configuration is that the peak throat surface Mach numbers of 0.98 on the cowl surface and 1.04 on the hub surface for $M_{t,av}$ of 0.869 are sufficiently high to

suppress engine noise radiation through the inlet while the sonic inlet still maintains a fairly high total pressure recovery of 0.970. Significant engine noise reductions should be realized with this level of $M_{t,av}$.

Boundary-Layer Characteristics

This section presents and discusses both the reduced experimental turbulent-boundary-layer data and the theoretical predictions along the annulus walls. The experimental, turbulent-boundary-layer data reduction program as previously presented in the section Data Reduction uses the boundary-layer rake measurements and the passage survey rake measurements. The important boundary-layer assumptions used in this data reduction program are reiterated here:

(1) An empirical law-of-the-wall equation (eq. (9)) is used to determine the experimental skin friction coefficient.

(2) Static pressure across the boundary layer is constant.

(3) The method of construction of the boundary layer from rotational core flows is valid.

(4) In the annular straight section the flow is incompressible.

(5) The process of solving for U_e from Ludwieg and Tillman's empirical equation (eq. (15)) is valid and applicable for determining a new boundary-layer edge velocity as part of the general iteration procedure for U_e.

Applying this general calculation technique permitted a logical and consistent method for reducing the measured boundary-layer data.

The theoretical predictions consist of results calculated by using the differential turbulent-boundary-layer analysis of reference 5. Compressible-flow relations, along with the measured surface static pressure distributions, were used to determine the free-stream flow properties along the inlet. These free-stream flow properties, such as the surface Mach number distribution, were then used as input to the boundary-layer program of reference 5. One exception to this usual procedure for the 35-tapered-vane configuration was that the boundary-layer-edge flow properties along the surface downstream of the vanes were calculated by using the reduced total pressure (not the plenum pressure) from the boundary-layer data reduction program. This reduced total pressure reflects the total pressure loss caused by the choking vanes in the throat region. As discussed in the section Inlet Design, the theoretical turbulent-boundary-layer calculation was initially started near the stagnation point on the flight lip, and the boundary layer was assumed to be turbulent all along the inlet surface.

Comparison of diffuser design parameters with experimental results. - Comparing the design free-stream Mach number distribution along the cowl surface with the mea-

sured distribution in figure 27 shows a significantly different Mach number variation in the throat region. This different Mach number variation in the throat region for the design calculations resulted from using the geometric cross-sectional area of the vanes as the effective flow-blockage area. The true effective flow-blockage area also depends on the vane boundary layer and the effect of the trailing-edge wakes coming off the vanes. The measured free-stream Mach number distribution in figure 27 shows a more gradual increase just upstream of the geometric throat and a more gradual decrease downstream of the geometric throat than shown in the design distribution. This gradual measured Mach number distribution in the throat region essentially resulted in a more gradual form factor distribution than the original design distribution for the form factor (fig. 27). For interest, figure 27 also gives the Mach number distribution after the vanes that was determined by using the reduced total pressure from the boundary-layer data reduction program. This reduced total pressure, which reflects the total pressure loss of the vanes, was assumed to occur immediately downstream of the vanes. In summary, the measured free-stream Mach number and form factor distributions were shifted somewhat from the design distributions, but the concept of controlling the velocity (Mach number) gradient (and thereby the boundary-layer form factor) by the wavy-wall type of geometry worked very well (figs. 27 and 17). This design concept of controlling the diffuser velocity gradient with the proper wavy-wall type of geometry may be useful as a guideline for minimizing the total pressure losses as well as for preventing boundary-layer separation in any diffusion process.

Comparison of calculated and experimental boundary-layer parameters. - The reduced turbulent-boundary-layer data and theoretical calculation results are presented as a function of the axial distance from the geometric throat and also as a function of the average throat Mach number. In this way, the rapid boundary-layer growth along the diffuser can be described; and also the effect of large flow changes, represented by the average throat Mach number, can be shown for a given axial location where boundary-layer measurements were taken.

First, some general trends in the theoretical prediction will be discussed. In figures 28 to 30, theoretical distributions of the form factor H, the skin friction coefficient C_f, and displacement thickness δ^* are presented as functions of the inlet axial distance from the geometric throat for the takeoff (no vane) configuration. Similarly, distributions of H, C_f, and δ^* are presented in figures 31 to 33 for the landing (35 tapered vane) configuration. Comparing figures 28 and 31 shows the most obvious difference in the inlet distribution of the form factor H to be that the large-peak type of behavior of H just after the vanes for the 35-tapered-vane configuration is completely absent for the no-vane configuration. This behavior reflects the surface Mach number distributions shown in figures 20 and 24. Note from figure 28 that for operation at $M_{t,\,av} \geq 0.917$, for which the total pressure recovery was 0.988 or greater, the H was

under 1.9. For operation at $M_{t,av}$ of 0.947, at which the total pressure recovery had begun to decrease sharply, the H became greater than 2.0 at several locations, with a peak value of 2.16. From figure 29 the skin friction coefficient C_f for $M_{t,av}$ of 0.947 reached a minimum value of 0.0003 at the same axial location as the peak H value.

For the 35-tapered-vane configuration the theoretical H along the diffuser is characterized by the large-peak type of distribution in the throat region, which is especially pronounced at large values of $M_{t,av}$ (fig. 31). Over the high-total-pressure-recovery (>0.970) operating range, which is covered by $M_{t,av}$ of 0.843 and below, peak H values of 2.03 or less are indicated in figure 31. For an $M_{t,av}$ of 0.899, where the total pressure recovery has already begun to decrease sharply, the peak H value is 2.24 and the minimum C_f from figure 32 is approximately 0.0004. At the largest values of $M_{t,av}$ shown for both the no-vane and 35-vane configurations, large boundary-layer losses will occur as indicated by the low total pressure recovery (fig. 16) and the large increase in the boundary-layer displacement thickness δ^* (figs. 30 and 33). From the measured total pressure recovery and the theoretical predictions of H, a guideline for high total pressure recovery in future diffuser designs is to keep $H \leq 2.0$ for the wall boundary layer.

Boundary-layer rake measurements were taken at stations 19 and 20 (fig. 11). Both axial locations (stations 19 and 20) are in the straight annulus region downstream of the diffuser section. Before the experimental boundary-layer data are compared with theoretical predictions, some discussion of the measured, nonequilibrium, turbulent-boundary-layer flow in the annular straight section is needed. As the flow enters the annular straight section, the turbulent boundary layer, which has experienced a severe adverse pressure gradient in the diffuser, now suddenly encounters a zero pressure gradient. This type of sharply decreasing pressure gradient has been shown by Bradshaw and Ferris (ref. 13) to produce a strong nonequilibrium turbulent boundary layer. Reference 13 contains detailed turbulent-boundary-layer measurements for a relatively low-velocity, constant, adverse-pressure-gradient flow passing into a region of zero pressure gradient. Bradshaw and Ferris (ref. 13) have determined that the resulting nonequilibrium turbulent boundary layer in the zero-pressure-gradient region is controlled by the advection of turbulent kinetic energy from the adverse-pressure-gradient region. They concluded that the turbulent shear stress cannot be defined by the usual local conditions (velocity gradient and mixing length) across the boundary layer. Since most theoretical analyses, like reference 5, assume that the turbulent shear stress can be determined from the local velocity gradient and the mixing length theory, good agreement of these theories cannot be expected for this nonequilibrium turbulent-boundary-layer region. Nevertheless, the following general comparisons of theory with

data are made from figures 28 to 33 for the turbulent boundary layer in the straight-annular-section, tapered, vane configurations:

(1) Large differences between the theoretical and experimental values of H and C_f are apparent for high $M_{t,av}$. At low $M_{t,av}$, these differences are reduced.

(2) The theoretical δ^* shows fair agreement with the experimental data.

The following comparison of theoretical and measured turbulent-boundary-layer results indicates some of the differences that can exist when equilibrium-boundary-layer solution techniques are used to calculate a nonequilibrium boundary layer. Figures 34 and 35 present the turbulent-boundary-layer velocity profiles at an axial location (station 19) just 3 centimeters after the diffuser and at the fan entrance (station 20), which is 20 centimeters after the diffuser. From figures 34 and 35, comparing the experimental and theoretical turbulent-boundary-layer velocity profiles shows a much steeper (fuller) velocity profile for the experimental data (takeoff no-vane configuration) at both measurement stations (19 and 20). This same result occurred for the 35-tapered-vane configuration (figs. 36 and 37). Also the experimental skin friction coefficient C_f for both the no-vane and 35-tapered-vane configurations was significantly larger than the theoretical C_f throughout the range of $M_{t,av}$ (figs. 38 and 39). However, this trend of high experimental skin friction coefficient is consistent with the measured fuller velocity profiles, which produced a steeper velocity gradient at the wall so that the wall shear stress (hence, C_f) was higher than the theoretical results. In addition, the fuller velocity profiles correspond to an increase in the law-of-the-wall region of the boundary layer as clearly seen in figures 40 to 43, especially at the fan entrance. This increased law-of-the-wall region was accompanied by a large decrease in the "law-of-the-wake" outer region of the boundary layer; and that is the main reason for determining the experimental skin friction coefficient from only a law-of-the-wall model (as seen in figs. 40 to 43).

The greatest discrepancy between the theory and the data is shown from figures 38 and 39 to be in the form factor H for both the no-vane and 35-tapered-vane configurations. At the higher average throat Mach numbers, the experimental H suddenly decreased, which is the exact reverse of the theoretical H, which suddenly increased. As the velocity profile became much steeper, the form factor H actually decreased with increasing $M_{t,av}$ even though the boundary layer became thicker. In fact, the experimental displacement thickness was generally less at station 20 than at station 19 (figs. 20 and 26); and this shows the strong relaxation effect (steep velocity profile) on the boundary layer. Since the theoretical analysis (ref. 5) did not include any nonequilibrium relaxation effects on the boundary layer, the large theoretical H calculated for the strong adverse pressure gradient in the diffuser still remained quite high in the straight section and increased with $M_{t,av}$.

The experimental results of reference 13 also show this same extreme discrepancy

of H with theoretical predictions for the nonequilibrium turbulent boundary layer. In fact, reference 13 shows that the change of the experimental H with wall distance differed from the theoretical predictions by more than an order of magnitude.

From figures 22 and 26 the theoretical momentum thickness also agrees poorly with experimental data at higher $M_{t, av}$. The theoretical displacement thickness δ^* is generally in fair agreement with the experimental data (figs. 22 and 26). However, this fair agreement of the theory with experimental data for δ^* was probably caused by the following compensating effects:

(1) A theoretical velocity profile that is not as steep as the experimental velocity profile, especially near the wall, would tend to give a larger theoretical displacement thickness.

(2) A smaller theoretical boundary-layer thickness than the experimental data would tend to produce a smaller theoretical displacement thickness.

SUMMARY OF RESULTS

The aerodynamic performance and boundary-layer characteristics of a solic inlet were determined without the fan in place for the takeoff (no vane) configuration and the four landing configurations: a 35-tapered-vane configuration, a 35-constant-thickness-vane configuration, a 54-tapered-vane configuration, and a 54-slanted-and-tapered-vane configuration.

Experimental total pressure distributions were measured at the fan entrance station and used to determine the inlet total pressure recovery, the radial total pressure distribution, and the turbulent-boundary-layer velocity profiles. Static pressure distributions along the annulus walls were used to calculate the surface Mach numbers. Analyzing the reduced experimental data gave the following results:

1. The sonic inlet with the 35-tapered-vane configuration produced the best overall total pressure recovery of all vane configurations over the complete range of the normalized average throat Mach number $M_{t, av}$.

2. For the takeoff (no vane) configuration, a high total pressure recovery (0.988) was obtained with peak surface Mach numbers in the throat region of 1.07 on the cowl surface and 0.99 on the hub surface at $M_{t, av}$ of 0.917.

3. For the landing (35 tapered vane) configuration, a high total pressure recovery (0.970) was obtained with peak surface Mach numbers in the throat region of 0.98 on the cowl surface and 1.04 on the hub surface at $M_{t, av}$ of 0.869.

4. From the measured distributions and theoretical predictions a guideline for high total pressure recovery in future diffuser designs is to keep the form factor $H \leq 2.0$ for the wall boundary layer.

5. The concept of controlling the velocity gradient in the diffuser with a specially designed wavy-wall type of diffuser geometry not only prevented turbulent-boundary-layer separation but also tended to minimize the total pressure losses.

6. As the flow passed from the strong adverse pressure gradient of the diffuser into the zero-pressure-gradient straight section, a severe nonequilibrium relaxed boundary layer was formed for which the measured velocity profiles, the form factor H, and the skin friction coefficient C_f were greatly different than the theoretical predictions.

Lewis Research Center,
National Aeronautics and Space Administration,
Cleveland, Ohio, June 10, 1976,
505-04.

APPENDIX - SYMBOLS

A	area
A_{eff}	effective geometric throat area
A_{tt}	total geometric throat area
A_{vb}	blocked throat area of vanes
C_f	skin friction coefficient
c	chord
H	form factor, eq. (14)
M	Mach number, eq. (18)
$M_{t,av}$	average throat Mach number
$M_{t,n}$	normalized throat Mach number, eq. (5)
n_v	number of vanes
P	total pressure
P_{aa}	area-weighted, average total pressure, eq. (7)
Pr	Prandtl number
p	static pressure
R	universal gas constant
R_c	total pressure recovery, eq. (6)
r	inlet radius
T	total temperature
t	static temperature
t_v	vane thickness
U	velocity
U^+	dimensionless shear velocity, eq. (9)
W	distance to centerline
W_m	weight flow, eq. (1)
X	inlet axial distance
Y	boundary-layer distance from wall
Y^+	wall distance parameter, eq. (10)

γ	ratio of specific heats
δ^*	displacement thickness, eq. (13)
θ	momentum thickness, eq. (12)
μ	dynamic viscosity
ρ	density
τ	shear velocity

Subscripts:

aw	adiabatic wall condition
b	boundary layer
c	cowl surface
e	edge-of-boundary-layer condition
h	hub surface
inv	inviscid flow
m	measured quantity
max	maximum
ref	reference temperature condition, eq. (16)
t	throat
v	vane
w	wall condition
0	plenum condition

REFERENCES

1. Chestnutt, David: Noise Reduction by Means of Inlet-Guide-Vane Choking in an Axial Flow Compressor. NASA TN D-4682, 1968

2. Miller, Brent A.; and Abbott, John M.: Aerodynamic and Acoustic Performance of Two Choked-Flow-Inlets under Static Conditions. NASA TM X-2629, 1972.

3. Khijber, F.; et al.: Investigation of Noise Suppression by Sonic Inlets for Turbofan Engines. (D6-40855-Vol.-1, Boeing Commercial Airplane Co.; NAS3-15574) NASA CR-121126, 1973.

4. Ball, Calvin L.; Janetzke, David C.; and Reid, Lonnie: Performance of 1380-Foot-per-Second Tip Speed Axial Flow Compressor Rotor with Blade Tip Solidity of 1.5. NASA TM X-2379, 1971.

5. Albers, James A.; and Gregg, John L.: Computer Program for Calculating Laminar, Transitional, and Turbulent Boundary Layer for a Compressible Axisymmetric Flow. NASA TN D-7521, 1974.

6. Shapiro, Ascher H.: The Dynamics and Thermodynamics of Compressible Fluid Flow. Vol. I, The Ronald Press Co., 1953.

7. Van Dyke, Milton: Perturbation Methods in Fluid Mechanics. Academic Press, 1964, pp. 81-97.

8. Mellor, G. L.; and Wood, G. M.: An Axial Compressor End-Wall Boundary Layer Theory. ASME Paper 70-GT-80, 1970.

9. Schlichting, Herman (J. Kestin, trans.): Boundary Layer Theory. 2nd ed., McGraw-Hill Book Co., Inc., 1955.

10. Sasman, Philip K.; and Cresci, Robert J.: Compressible Turbulent Boundary Layer with Pressure Gradient and Heat Transfer. AIAA J., vol. 4, no. 1, Jan. 1966, pp. 19-25.

11. Eckert, Ernst R. G.: Survey on Heat Transfer at High Speeds. WADC TR-54-70, Weight Air Development Center, 1954.

12. Kazin, S. B.; and Mishler, R. B.: Single-Stage, Low Noise, Advanced Technology Fan. Volume III - Acoustic Design. (R76AEG259, General Electric Co.; NAS3-16813) NASA CR-134803, 1976.

13. Bradshaw, P.; and Ferriss, D. H.: The Response of a Retarded Equilibrium Turbulent Boundary Layer to the Sudden Removal of Pressure Gradient. NPL-AERO-1145, Natl. Phys. Lab. (ARC-26758; FM-3577; AD-469346), 1965.

TABLE I. - AERODYNAMIC INLET PERFORMANCE

(a) No vanes; design flow, 33.20 kg/sec

Weight flow, W_m, kg/sec	Average throat Mach number, $M_{t,av}$	Total pressure recovery, P_{aa}/P_0
17.43	0.323	0.9986
27.33	.578	.9951
31.60	.770	.9932
32.70	.865	.9897
33.04	.917	.9879
33.13	.939	.9853
33.16	.947	.9610
33.13	.939	.9355

(b) 35 Vanes; design flow, 26.60 kg/sec

Weight flow, W_m, kg/sec	Average throat Mach number, $M_{t,av}$	Total pressure recovery, P_{aa}/P_0
12.01	0.270	0.9976
19.15	.470	.9941
25.16	.741	.9847
26.25	.843	.9762
26.44	.869	.9697
26.56	.889	.9309
26.61	.899	.8289
-----	-----	------

(c) 54 Vanes; design flow, 23.27 kg/sec

Weight flow, W_m, kg/sec	Average throat Mach number, $M_{t,av}$	Total pressure recovery, P_{aa}/P_0
10.34	0.267	0.9965
17.71	.511	.9904
21.41	.703	.9815
22.41	.788	.9705
22.71	.822	.9434
22.92	.853	.9087
22.94	.856	.8455
-----	-----	------

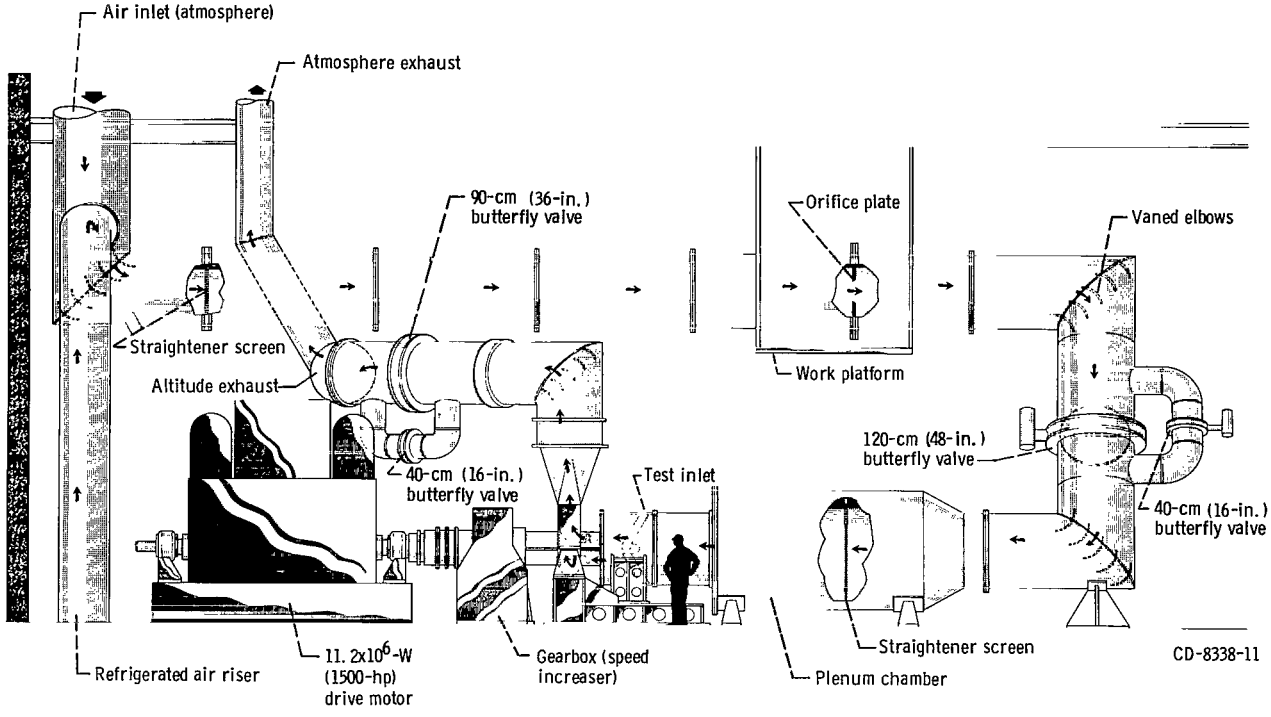

Figure 1. - Compressor test facility.

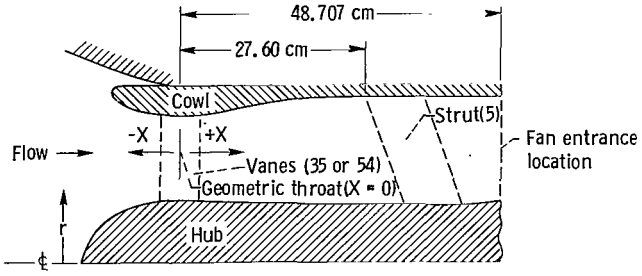

Cowl surface	
X, cm	r, cm
-10.287	26.454
-10.161	26.055
-9.525	25.184
-8.890	24.719
-7.620	24.133
-6.350	23.736
-5.080	23.446
-3.810	23.216
-2.540	23.038
-1.270	23.012
0	22.987
1.270	23.012
2.540	23.063
3.810	23.165
4.780	23.216
6.761	23.360
8.336	23.515
9.858	23.706
11.982	23.973
13.970	24.287
19.258	24.877
21.519	25.143
22.789	25.303
25.329	25.540
26.492	25.654
27.305	25.654
48.707	25.654

Hub surface	
X, cm	r, cm
-14.300	0
-13.970	1.748
-12.700	4.379
-11.430	5.730
-10.160	6.706
-8.890	7.447
-7.620	8.065
-6.350	8.545
-5.080	8.903
-3.810	9.192
-2.540	9.373
-1.270	9.479
0	9.525
17.780	[a]8.890
20.726	8.890
43.586	8.890
44.856	8.981
46.126	9.093
47.422	9.266
48.057	9.360
48.707	9.462

[a]Linear variation of r from X = 0 to 17.780.

Figure 2. - Sonic-inlet coordinates.

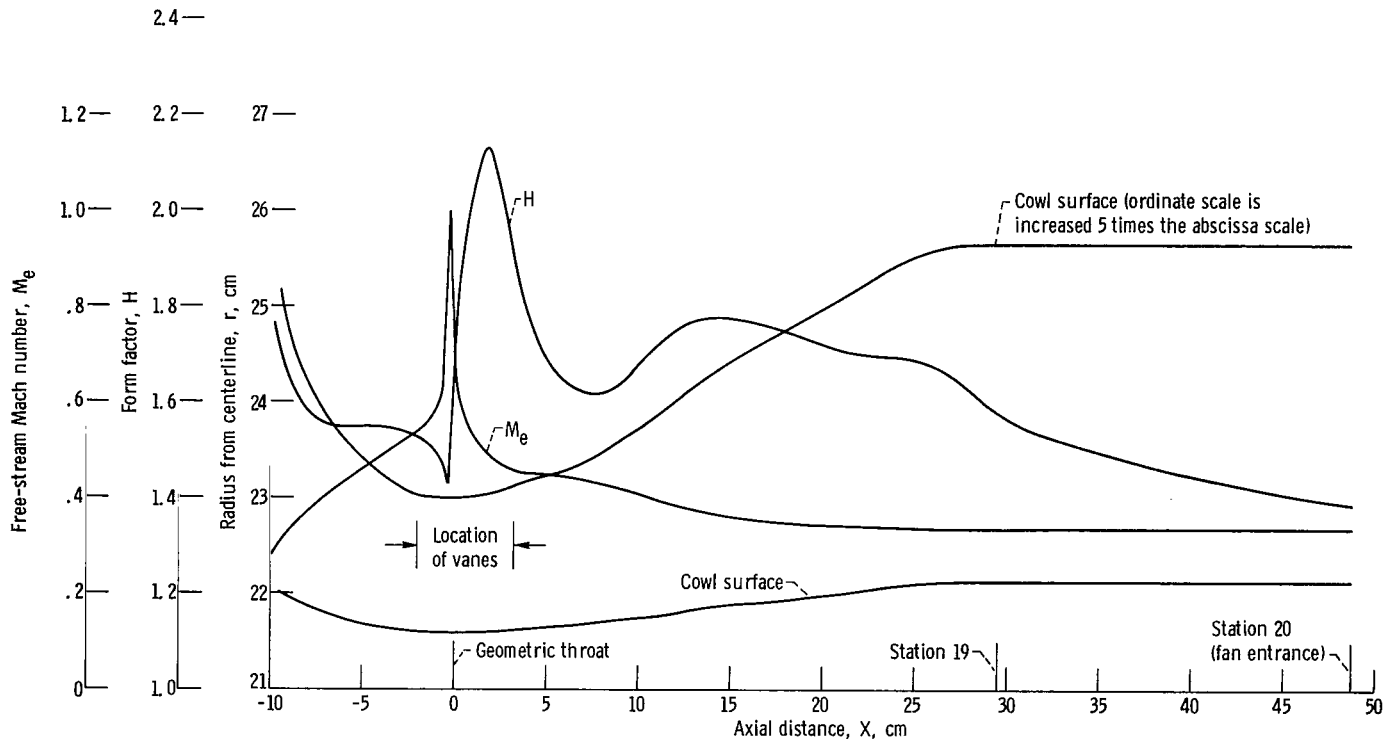

Figure 3. - Graphical detailed description of cowl surface (final design) and variation of design form factor and Mach number along cowl surface at average throat Mach number of 0.845 for landing configuration (35 vanes; tapered thickness).

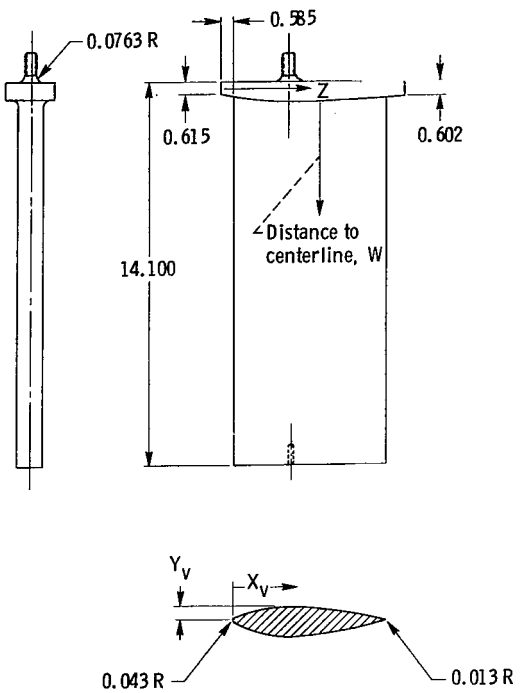

Vane profile chart	
X_V	Y_V
0	0
.0279	.0465
.0432	.0564
.0711	.0716
.1397	.0986
.2794	.1369
.4216	.1656
.5613	.1887
.8433	.2243
1.1227	.2494
1.4046	.2667
1.6840	.2771
1.9660	.2807
2.2454	.2771
2.5273	.2675
2.8067	.2525
3.0886	.2324
3.3680	.2085
3.6500	.1816
3.9294	.1522
4.2113	.1217
4.4907	.0909
4.7727	.0610
5.0521	.0338
5.3213	.0127
5.3340	0

Cowl profile chart	
Z	Distance to centerline, W
0	23.038
1.270	23.012
2.540	23.000
3.810	23.012
5.080	23.063
6.350	23.165

Figure 4. - Vane coordinates (constant thickness). Dimensions are in centimeters.

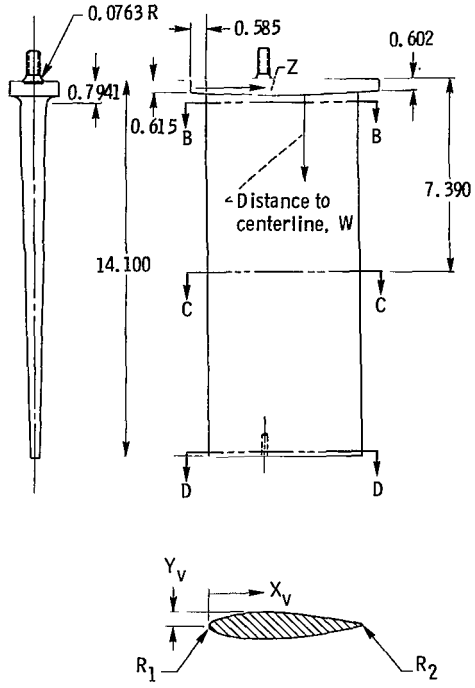

Vane profile chart

X_V	B-B Y_V (R_1 = 0.089; R_2 = 0.01275)	C-C Y_V (R_1 = 0.0432; R_2 = 0.01275)	D-D Y_V (R_1 = 0.01657; R_2 = 0.01275)
0	0	0	0
.0279	.0635	.0465	.0282
.0432	.0770	.0564	.0343
.0711	.0991	.0716	.0432
.1397	.1377	.0986	.0594
.2794	.1925	.1369	.0820
.4216	.2334	.1656	.0991
.5613	.2667	.1887	.1128
.8433	.3170	.2243	.1339
1.1227	.3531	.2494	.1491
1.4046	.3774	.2667	.1595
1.6840	.3917	.2771	.1659
1.9660	.3957	.2807	.1684
2.2454	.3896	.2771	.1669
2.5273	.3747	.2675	.1615
2.8067	.3515	.2525	.1529
3.0886	.3223	.2324	.1412
3.3680	.2878	.2085	.1323
3.6500	.2489	.1816	.1113
3.9294	.2075	.1522	.0937
4.2112	.1646	.1217	.0754
4.4907	.1219	.0909	.0566
4.7727	.0813	.0610	.0384
5.0521	.0447	.0338	.0216
5.3213	.0127	.0127	.0127
5.3340	0	0	0

Cowl profile chart

Z	Distance to centerline, W
0	23.038
1.270	23.012
2.540	23.000
3.810	23.012
5.080	23.063
6.350	23.165

Figure 5. - Vane coordinates (tapered thickness). Dimensions are in centimeters.

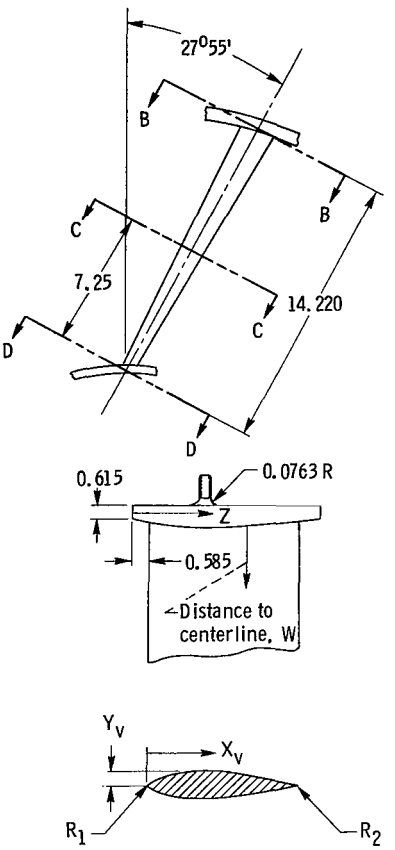

Vane profile chart			
X_V	B-B	C-C	D-D
	Y_V (R_1 = 0.0839; R_2 = 0.01275)	Y_V (R_1 = 0.0406; R_2 = 0.01275)	Y_V (R_1 = 0.0153; R_2 = 0.01275)
0	0	0	0
.0279	.0635	.0432	.0254
.0432	.0762	.0533	.0305
.0711	.0991	.0686	.0381
.1397	.1372	.0940	.0508
.2794	.1905	.1295	.0711
.4216	.2311	.1575	.0864
.5613	.2642	.1803	.0991
.8433	.3150	.2134	.1168
1.1227	.3505	.2388	.1295
1.4046	.3734	.2540	.1397
1.6840	.3886	.2642	.1448
1.9660	.3912	.2667	.1473
2.2454	.3861	.3642	.1448
2.5273	.3708	.2540	.1422
2.8067	.3480	.2413	.1346
3.0886	.3200	.2210	.1245
3.3680	.2845	.1981	.1118
3.6500	.2464	.1727	.0965
3.4294	.2057	.1448	.0813
4.2113	.1626	.1168	.0660
4.4907	.1219	.0864	.0483
4.7727	.0813	.0584	.0330
5.0521	.0457	.0330	.0178
5.3213	.0152	.0127	.0127
5.3340	0	0	0

Cowl profile chart	
Z	Distance to centerline, W
0	23.038
1.270	23.012
2.540	23.000
3.810	23.012
5.080	23.063
6.350	23.165

Figure 6. -Slanted vane coordinates (tapered thickness). Dimensions are in centimeters.

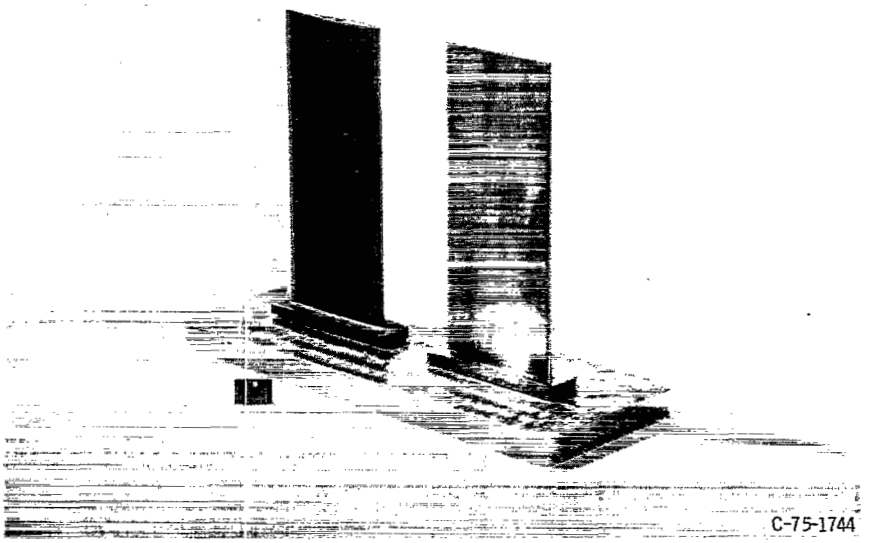

Figure 7. - View of tapered- and constant-thickness vanes.

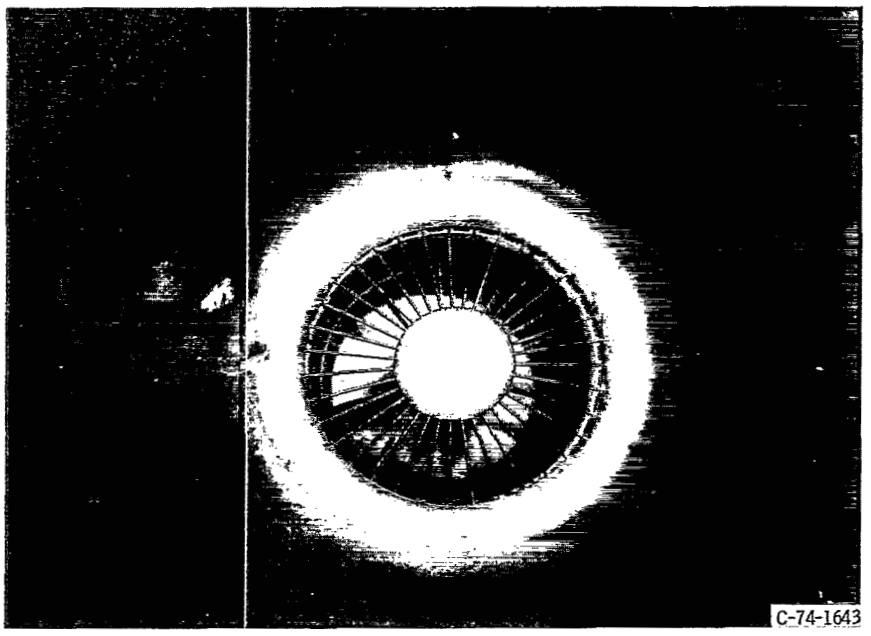

Figure 8. - 35-Tapered-vane configuration installed in sonic inlet.

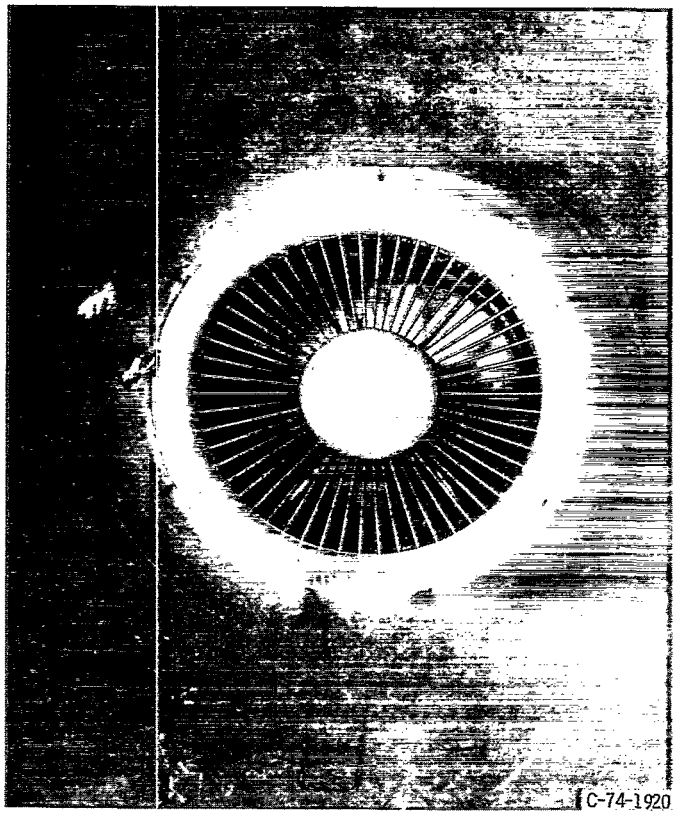

Figure 9. - 54-Tapered-vane configuration installed in sonic inlet.

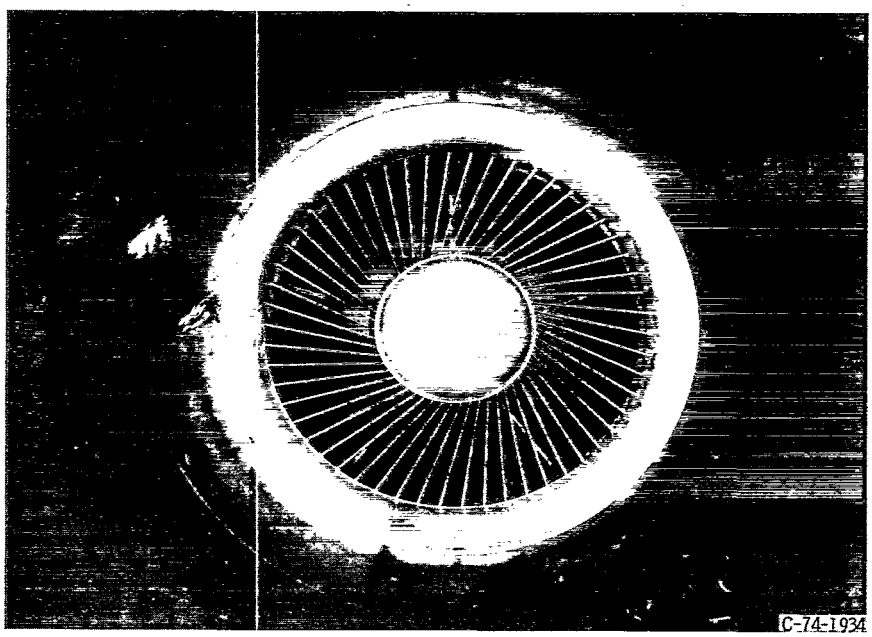

Figure 10. - 54-Tapered-and-slanted-vane configuration installed in sonic inlet.

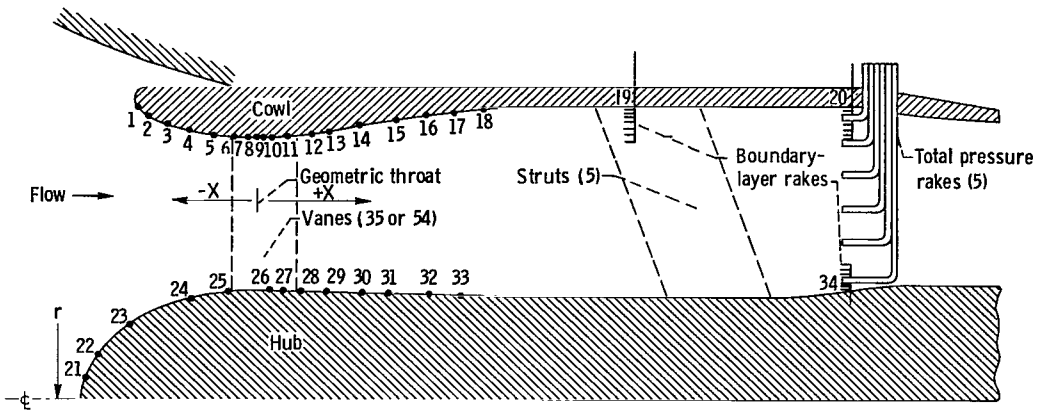

Cowl surface		
Static pressure tap station	Axial distance from geometric throat, X, cm	Radius from centerline r, cm
1	-10.160	26.055
2	-9.398	24.488
3	-7.366	24.067
4	-5.080	23.447
5	-3.175	23.114
6	-1.905	23.025
7	-.635	23.007
8	0	23.000
9	.635	23.007
10	1.270	23.012
11	2.540	23.063
12	4.602	23.216
13	5.796	23.282
14	7.676	23.444
15	10.818	23.835
16	13.970	24.293
17	16.718	24.602
18	20.320	24.983
[a]19	29.528	25.654
[b]20	48.707	25.654

Hub surface		
Static pressure tap station	Axial station from geometric throat, X, cm	Radius from centerline r, cm
21	-13.970	1.748
22	-12.700	4.379
23	-10.160	6.706
24	-5.080	8.903
25	-1.270	9.479
26	.635	9.500
27	1.270	9.462
28	2.540	9.423
29	5.080	9.322
30	5.890	9.195
31	11.430	9.093
32	13.970	8.992
33	17.145	8.890
[b]34	48.707	9.462

[a]Boundary-layer rake station
[b]Boundary-layer and total pressure rake station; fan entrance location.

Figure 11. - Sonic-inlet instrumentation.

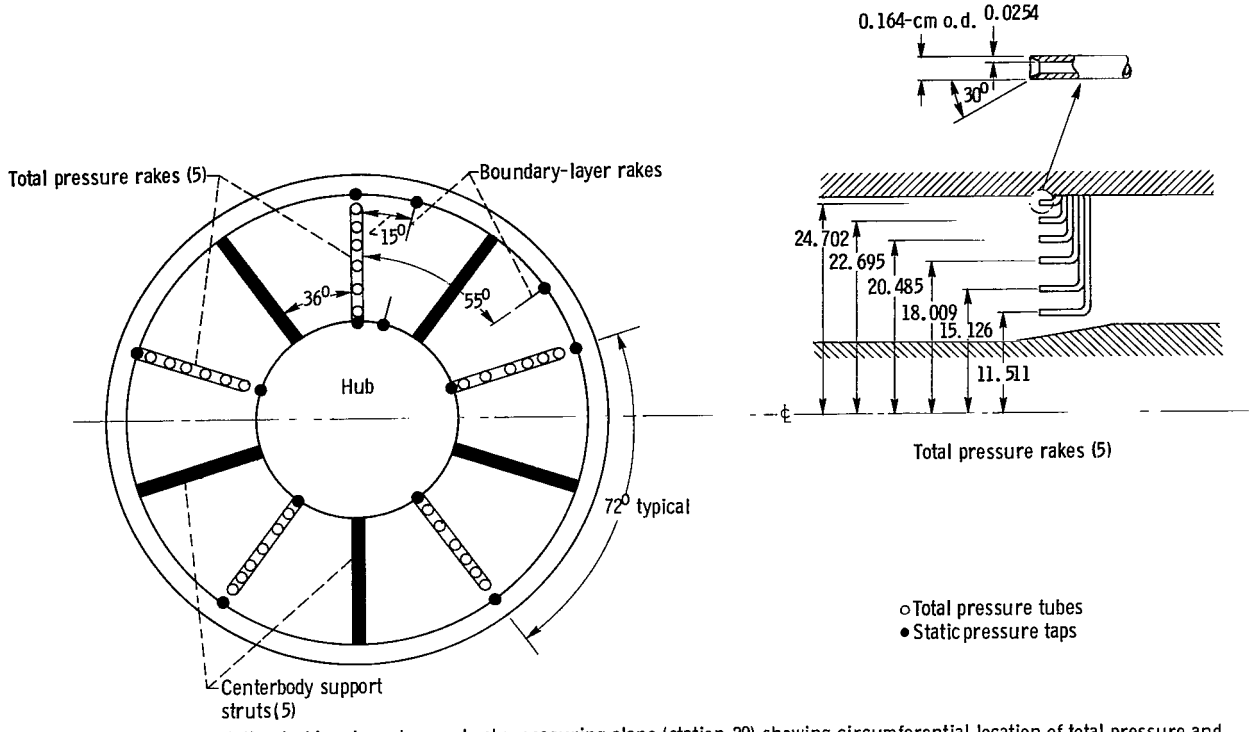

Figure 12. - Instrumentation looking downstream at rake measuring plane (station 20) showing circumferential location of total pressure and boundary-layer rakes and static pressure taps. Dimensions are in centimeters.

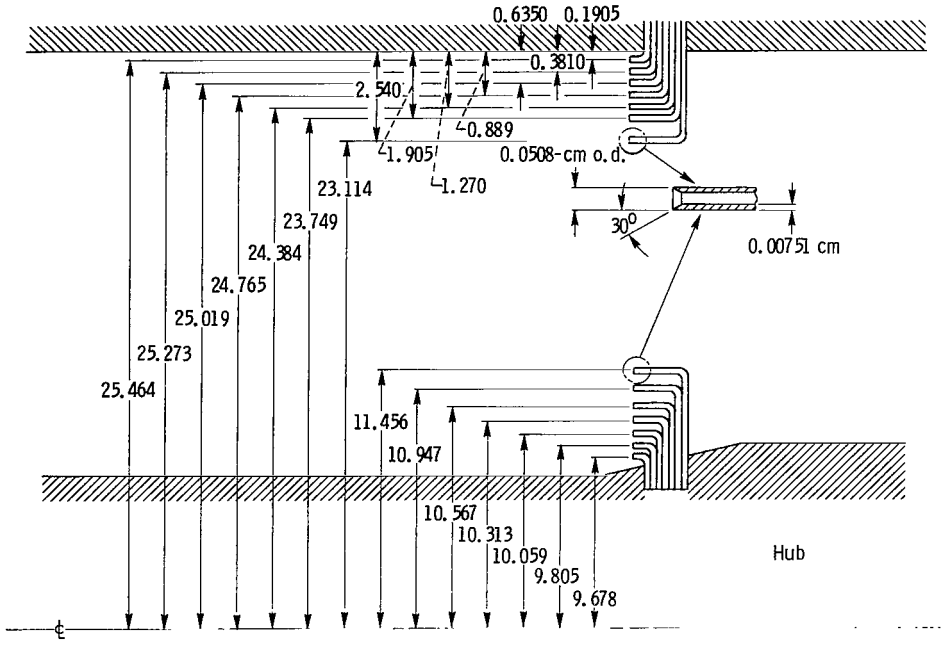

Figure 13. - Instrumentation schematic of boundary-layer rakes. Dimensions are in centimeters.

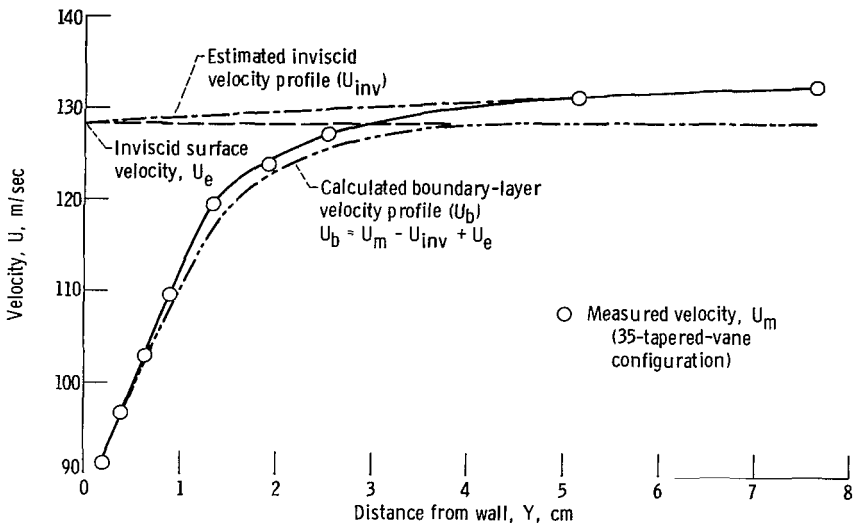

Figure 14. - Graphical description for "method of construction of the boundary layer from rotational core flows" applied to data for landing configuration (35 vanes; tapered thickness) on cowl surface (station 19) at average throat Mach number of 0.843.

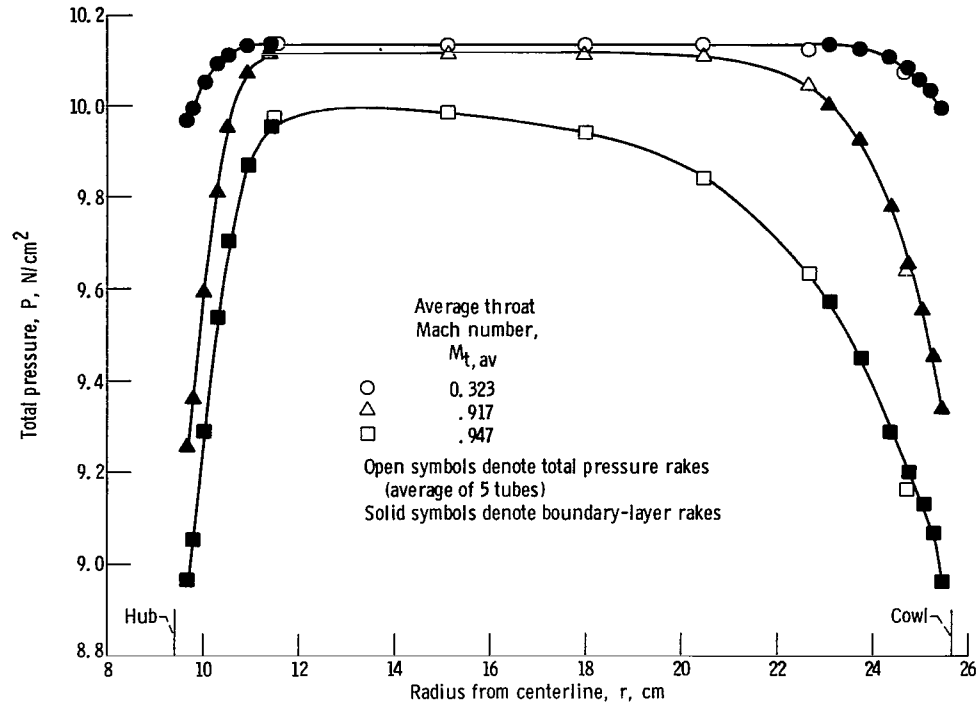

Figure 15. - Total pressure distribution from hub to cowl at fan entrance (station 20) for takeoff configuration (no vanes).

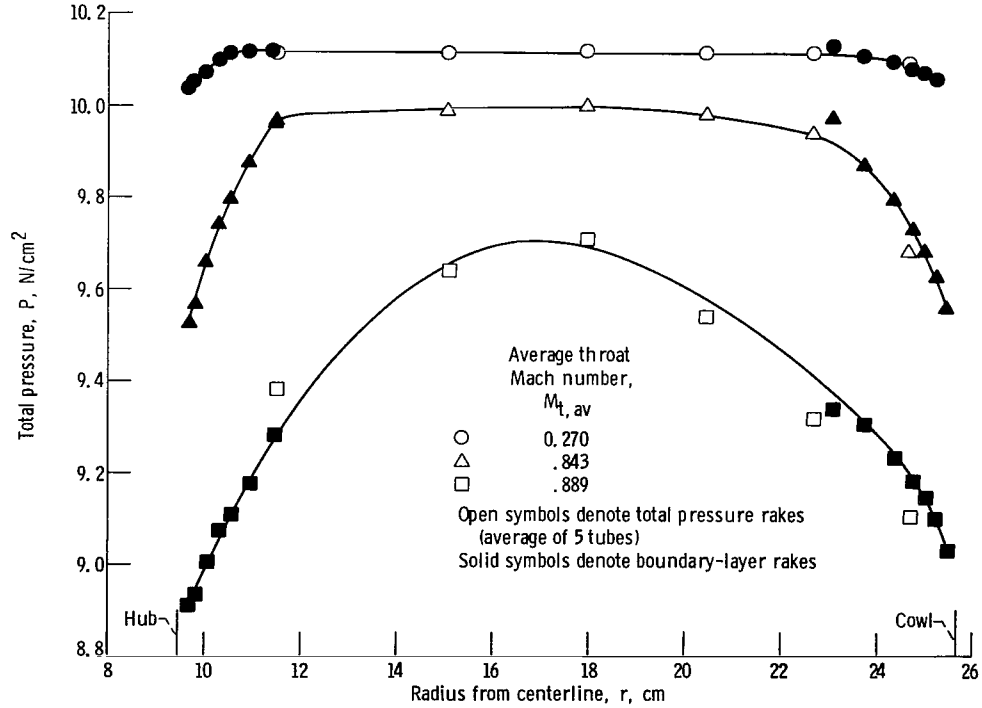

Figure 16. - Total pressure distribution from hub to cowl at fan entrance (station 20) for landing configuration (35 vanes; tapered thickness).

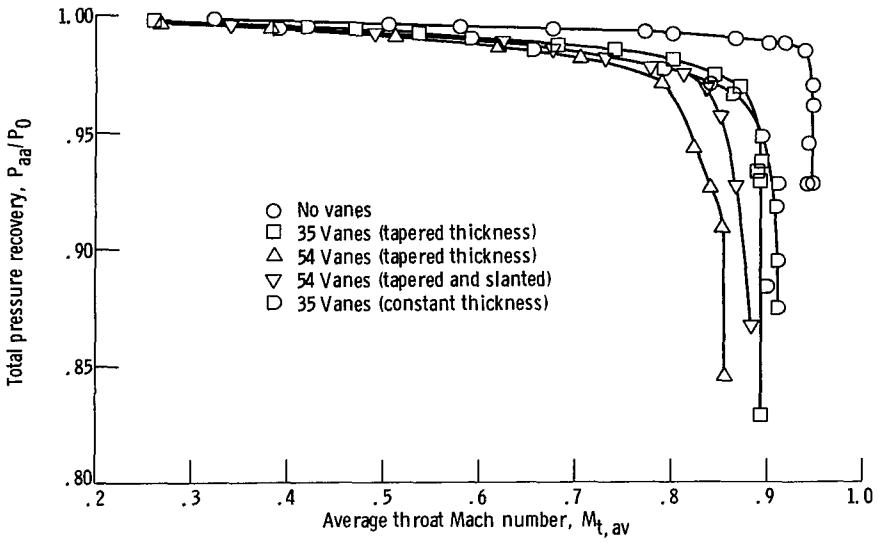

Figure 17. - Variation of total pressure recovery with average throat Mach number for sonic inlet with various radial-vane configurations.

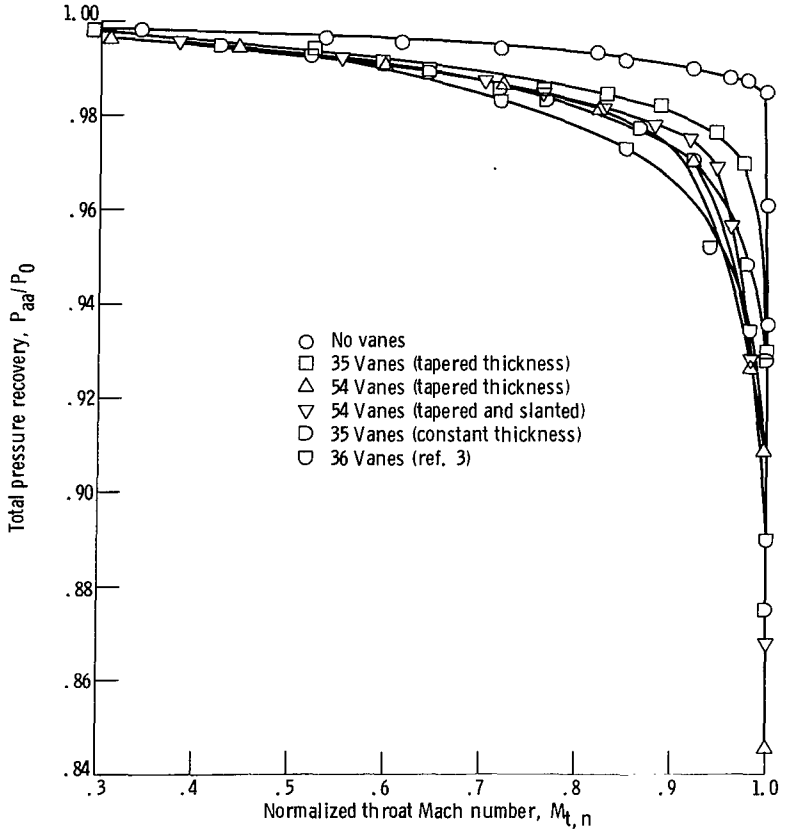

Figure 18. - Variation of total pressure recovery with normalized throat Mach number for sonic inlet with several radial-vane configurations.

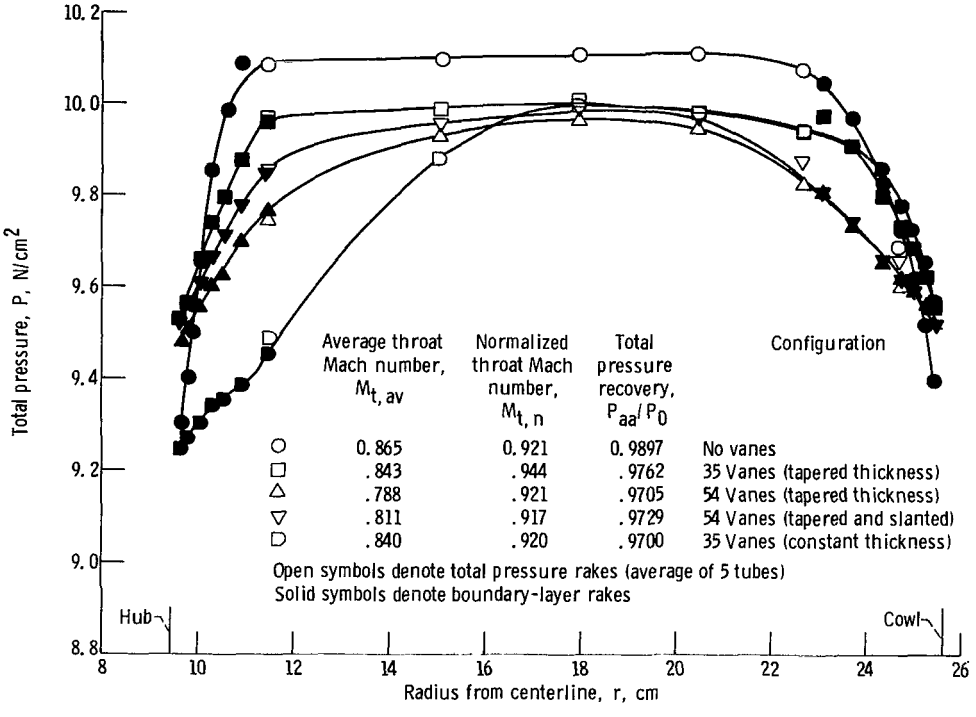

Figure 19. - Comparison of total pressure distributions from hub to cowl for several sonic-inlet configurations at fan entrance (station 20) with approximately the same normalized average throat Mach number.

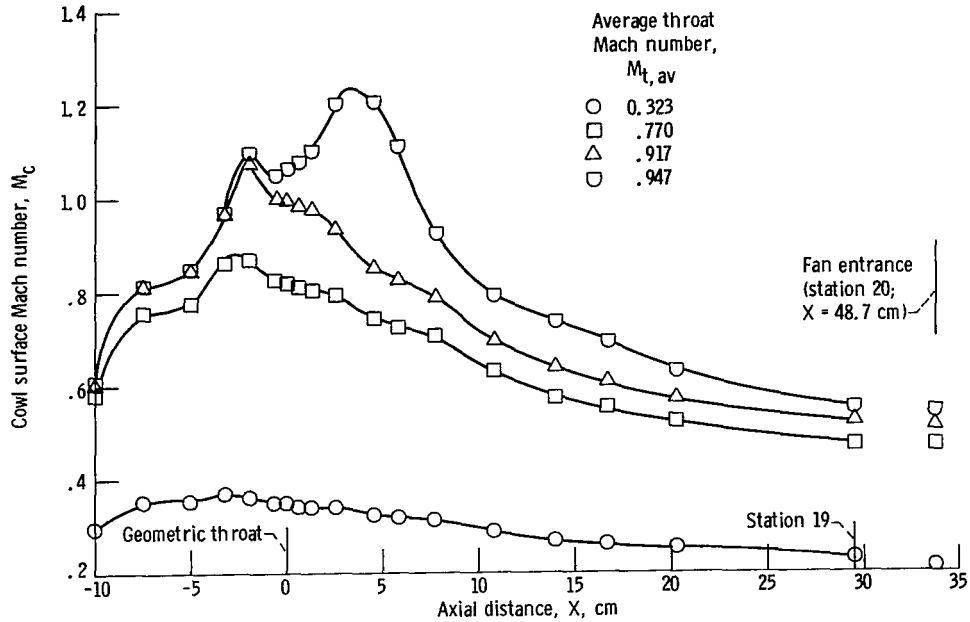

Figure 20. - Variation of cowl surface Mach number with axial distance from the geometric throat for takeoff configuration (no vanes).

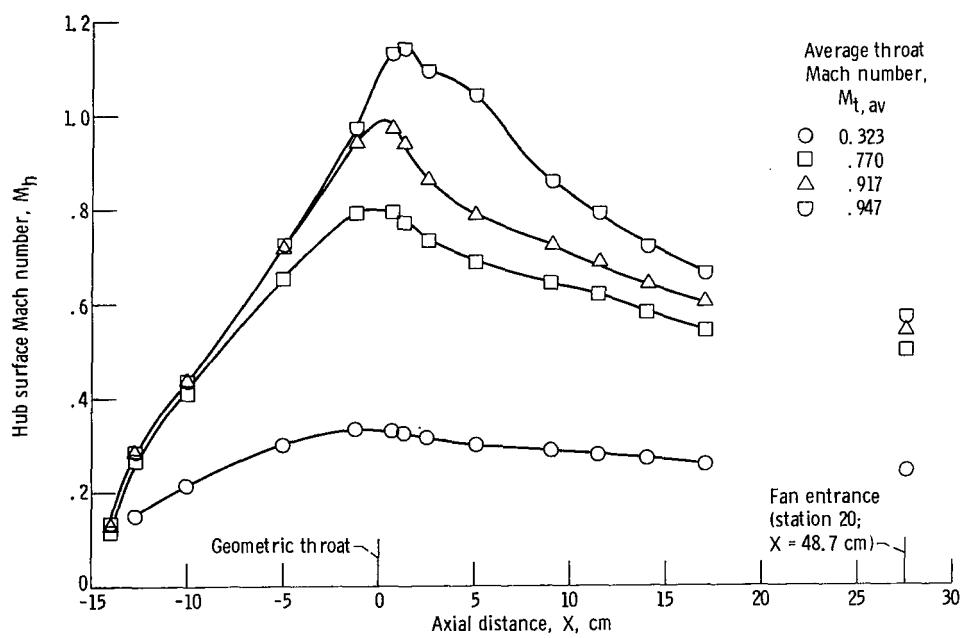

Figure 21. - Variation of hub surface Mach number with axial distance from geometric throat for takeoff configuration (no vanes).

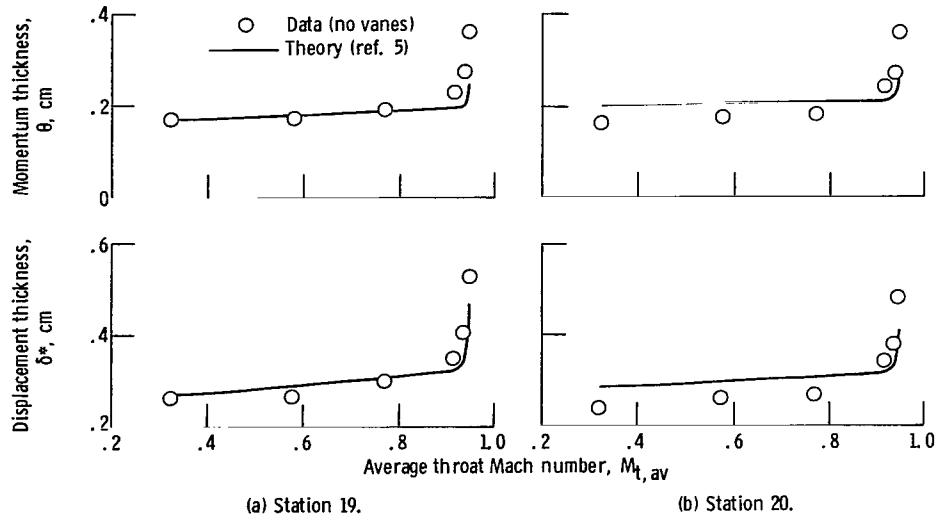

(a) Station 19. (b) Station 20.

Figure 22. - Variation of experimental momentum and displacement thicknesses along cowl surface with average throat Mach number and comparison with theoretical predictions for takeoff configuration (no vanes).

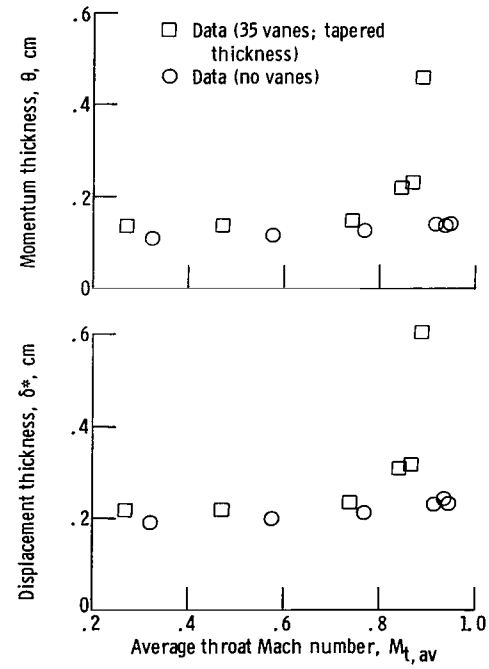

Figure 23. - Variation of experimental momentum and displacement thicknesses along hub surface with average throat Mach number at fan entrance (station 20).

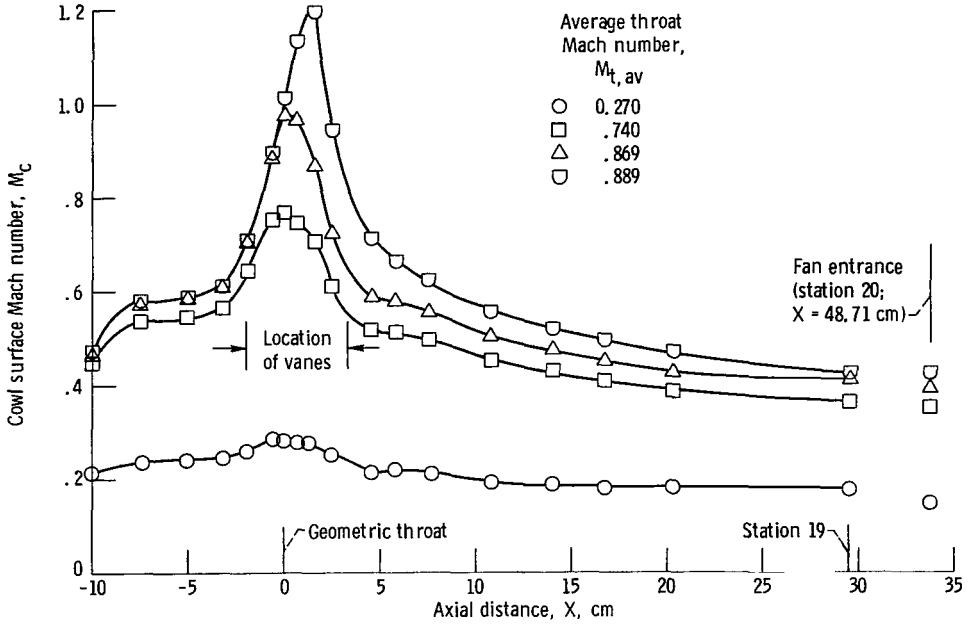

Figure 24. - Variation of cowl surface Mach number with axial distance from geometric throat for landing configuration (35 vanes; tapered thickness).

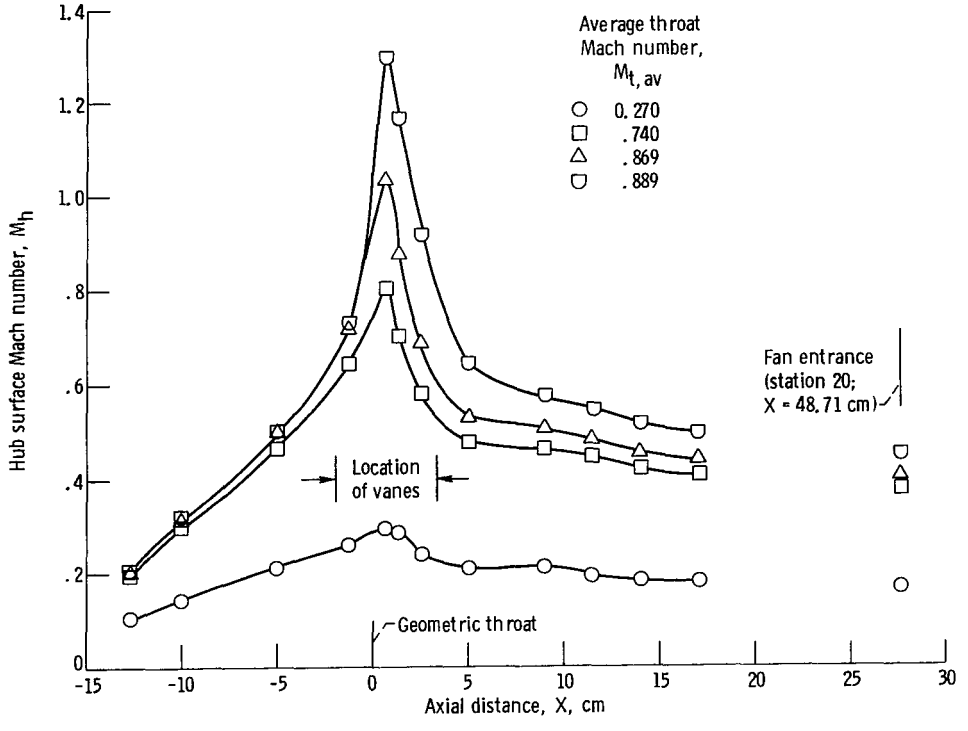

Figure 25. - Variation of hub surface Mach number with axial distance from geometric throat for landing configuration (35 vanes; tapered thickness).

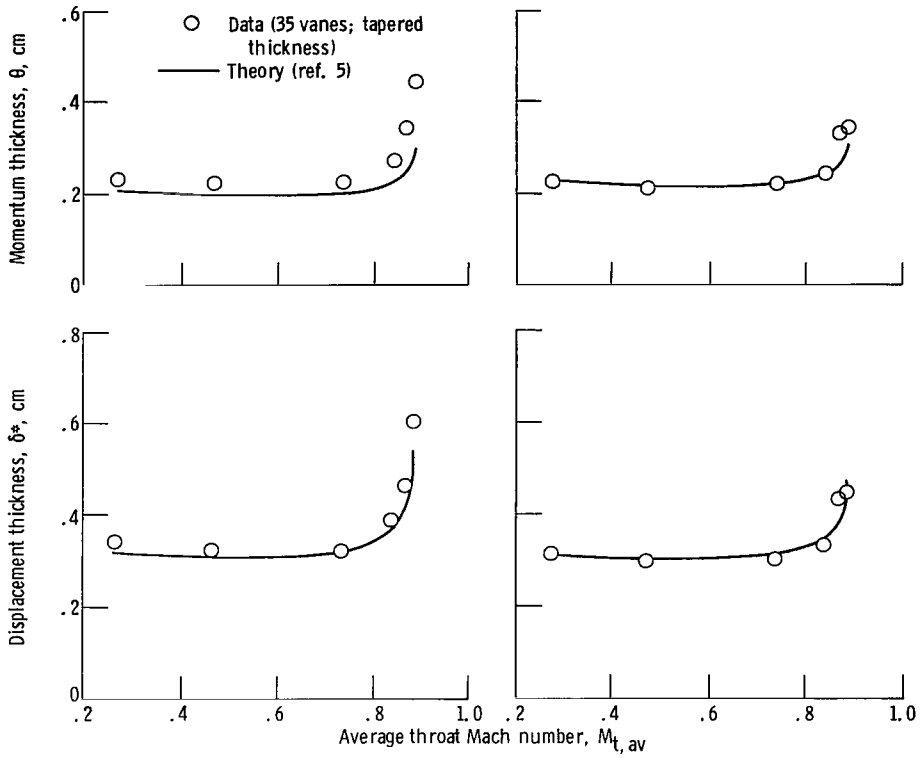

(a) Station 19. (b) Station 20.

Figure 26. - Variation of experimental momentum and displacement thicknesses along cowl surface with average throat Mach number and comparison with theoretical predictions for landing configuration (35 vanes; tapered thickness).

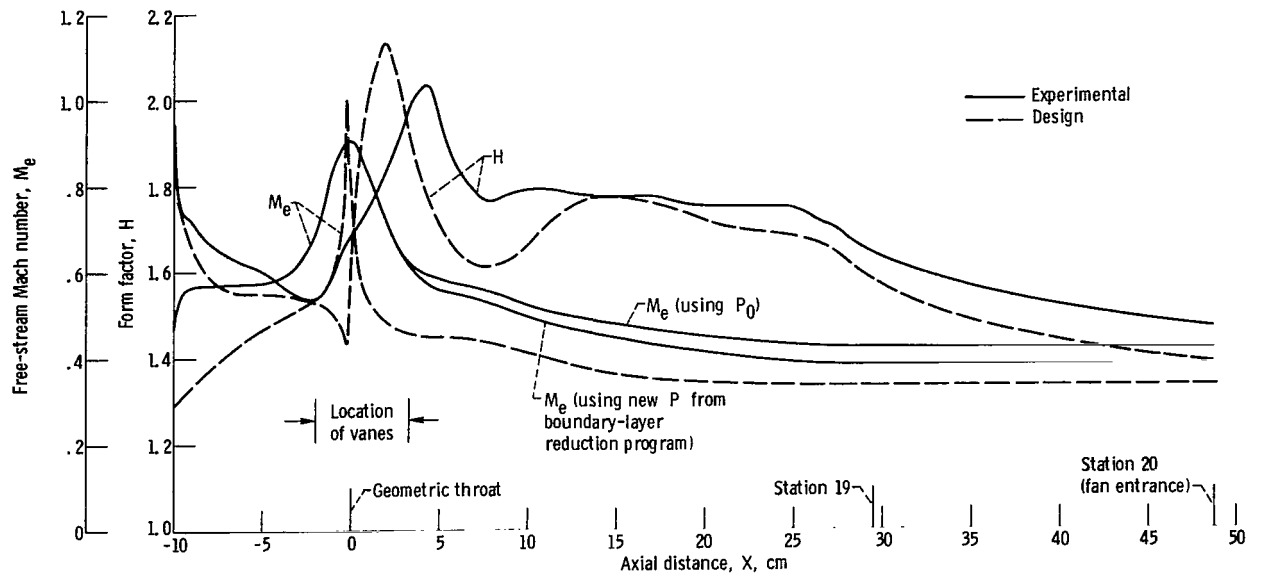

Figure 27. - Comparison of experimental form factor and Mach number with design prediction, along cowl surface, at average throat Mach number of 0.843 for landing configuration (35 vanes; tapered thickness).

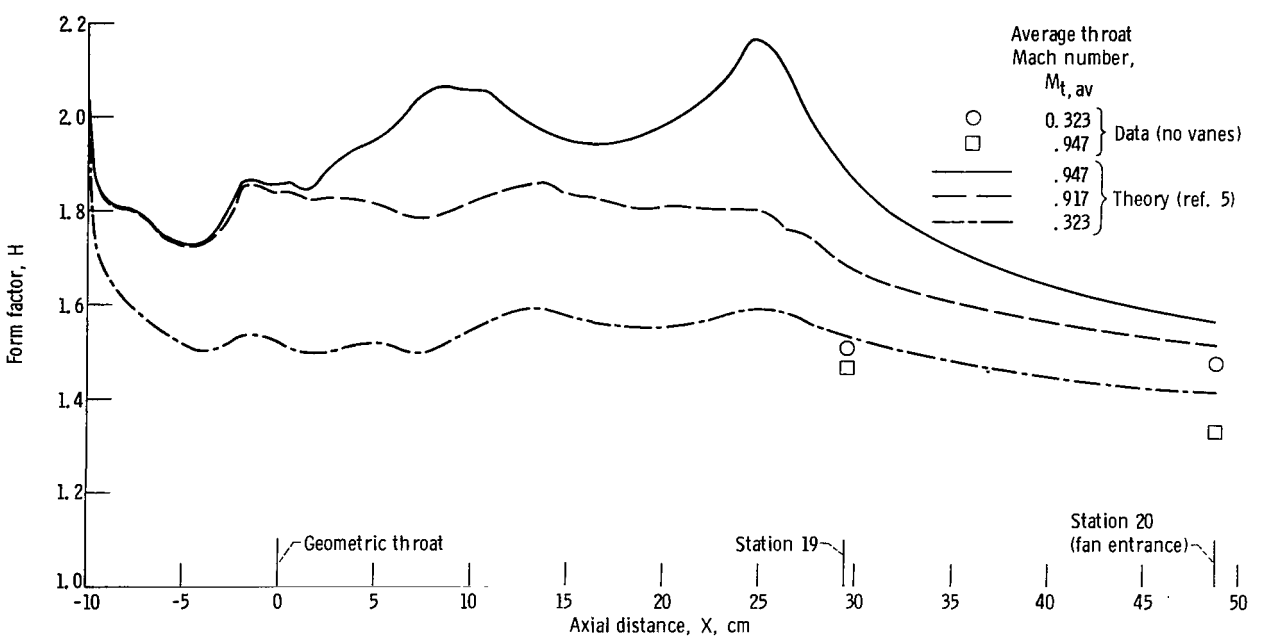

Figure 28. - Variation of form factor along cowl surface with axial distance from geometric throat for takeoff configuration (no vanes).

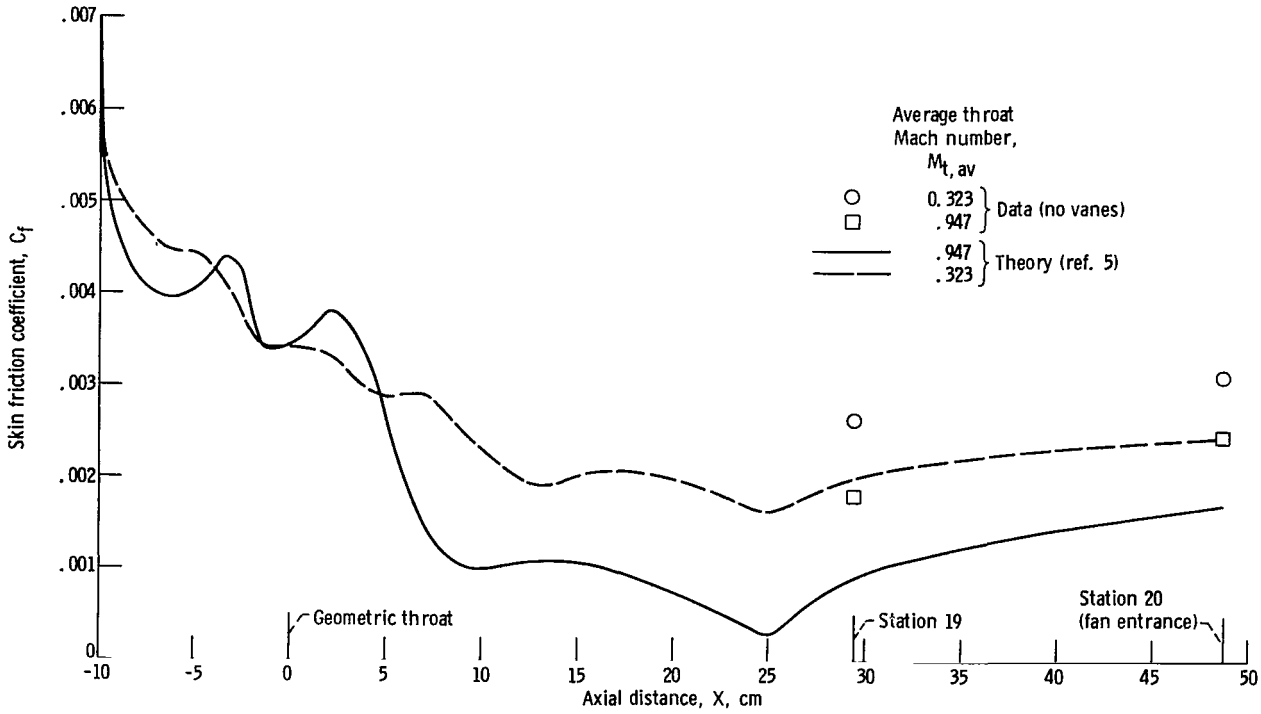

Figure 29. - Variation of skin friction coefficient along cowl surface with axial distance from geometric throat for takeoff configuration (no vanes).

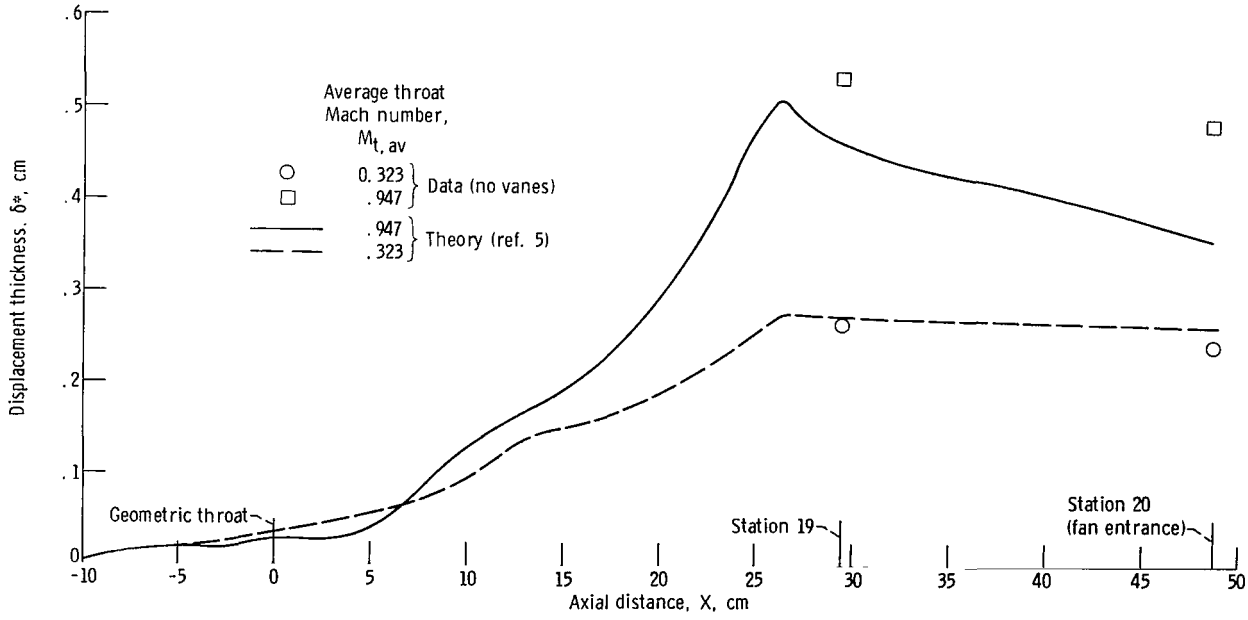

Figure 30. - Variation of displacement thickness along cowl surface with axial distance from geometric throat for takeoff configuration (no vanes).

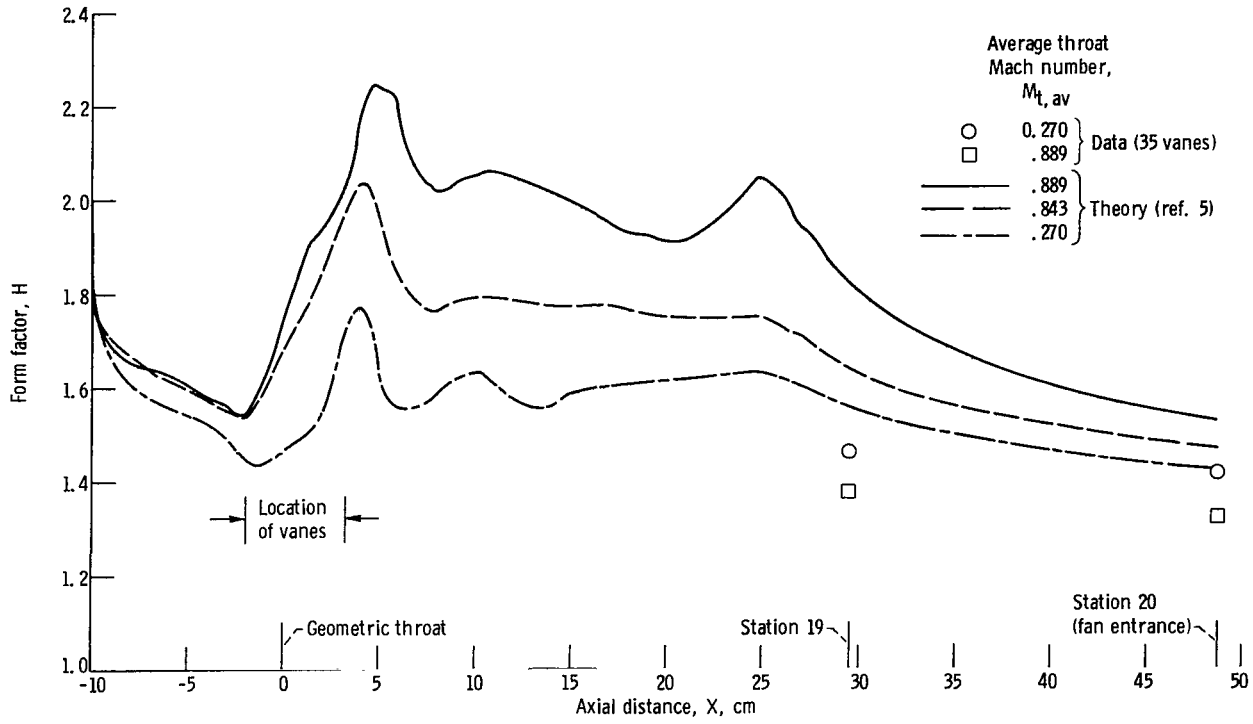

Figure 31. - Variation of form factor along cowl surface with axial distance from geometric throat for landing configuration (35 vanes; tapered thickness).

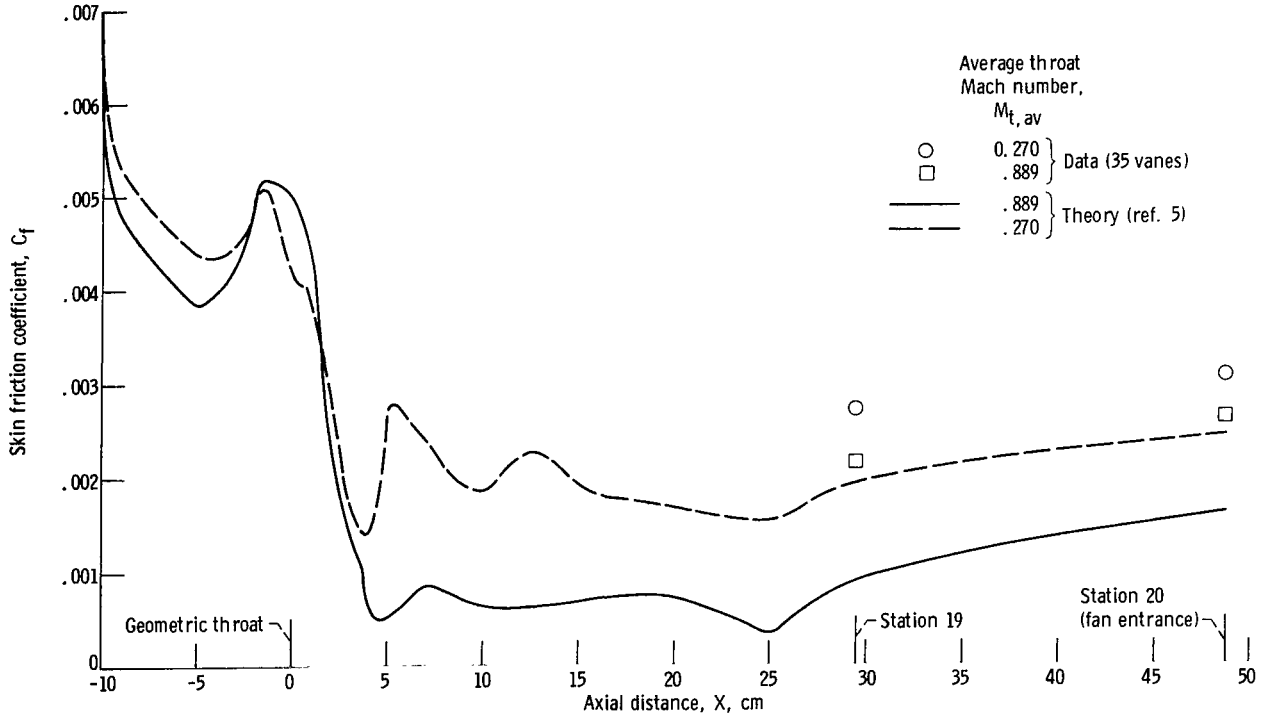

Figure 32. - Variation of skin friction coefficient along cowl surface with axial distance from geometric throat for landing configuration (35 vanes; tapered thickness).

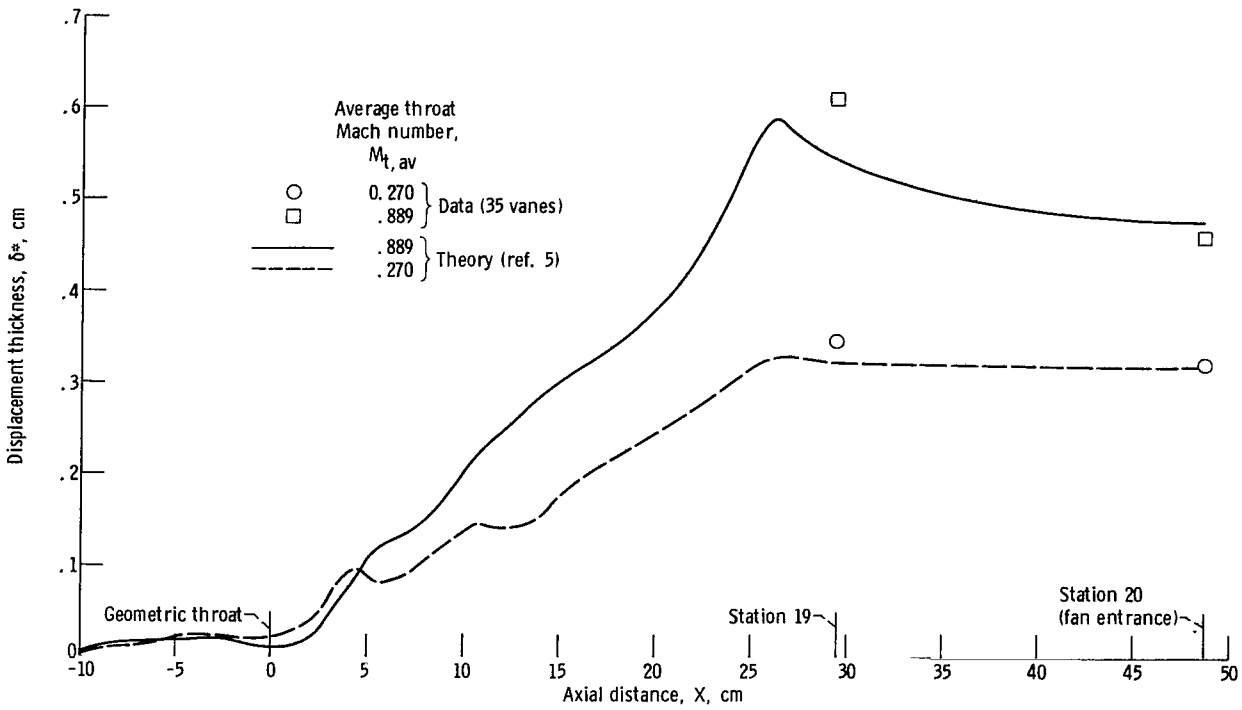

Figure 33. - Variation of displacement thickness along cowl surface with axial distance from geometric throat for landing configuration (35 vanes; tapered thickness).

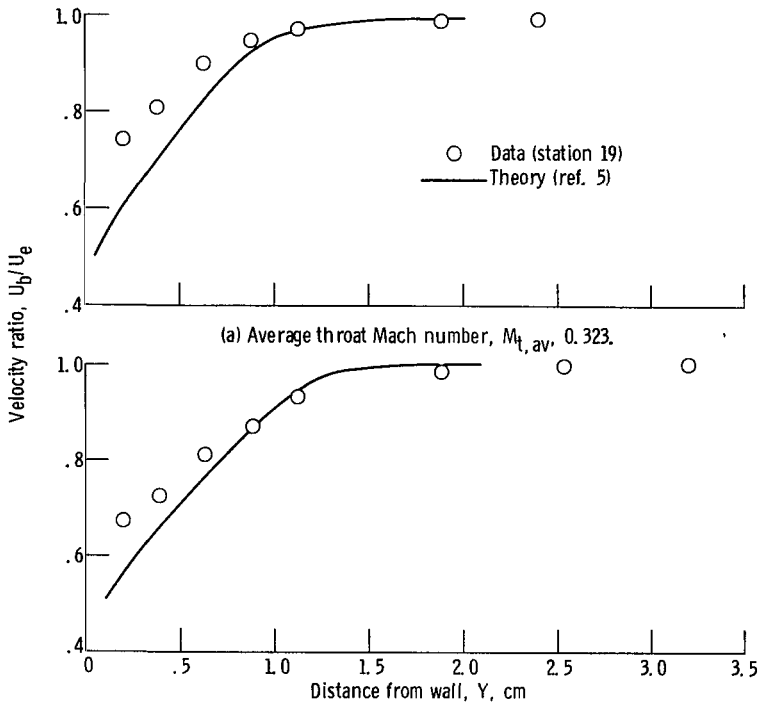

(a) Average throat Mach number, $M_{t,av}$, 0.323.

(b) Average throat Mach number, $M_{t,av}$, 0.917.

Figure 34. - Comparison of experimental boundary-layer velocity profiles along cowl surface (station 19) with theoretical predictions for takeoff configuration (no vanes).

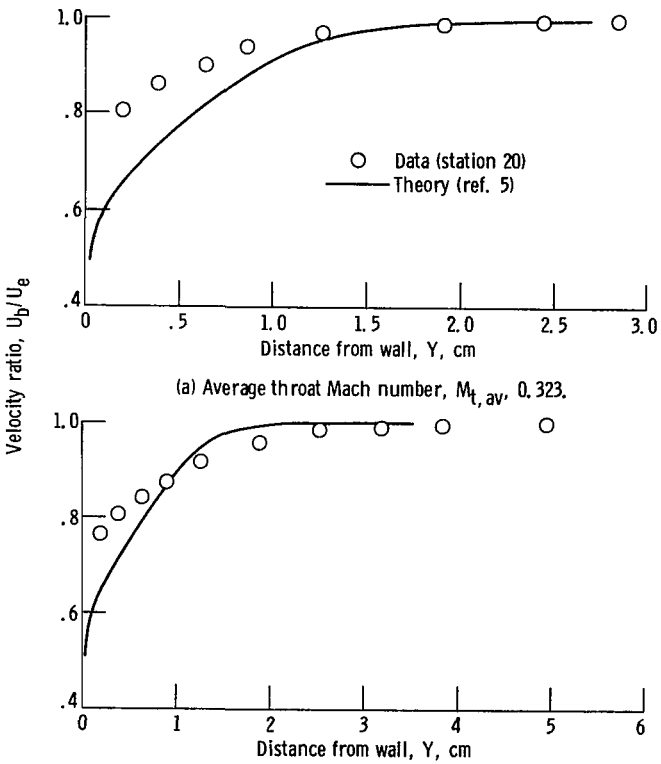

(a) Average throat Mach number, $M_{t,av}$, 0.323.

(b) Average throat Mach number, $M_{t,av}$, 0.917.

Figure 35. - Comparison of experimental boundary-layer velocity profiles along cowl surface (station 20) with theoretical predictions for takeoff configuration (no vanes).

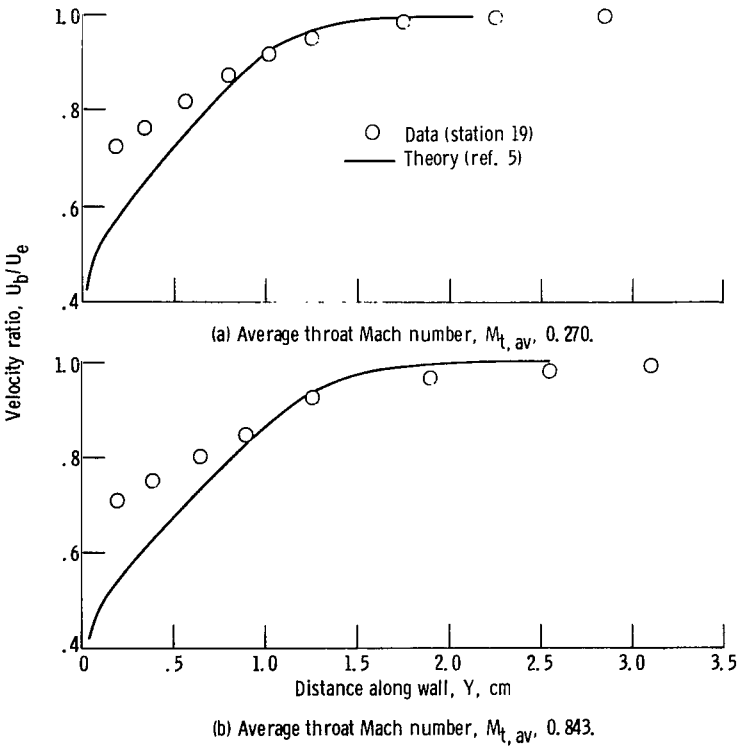

(a) Average throat Mach number, $M_{t,av}$, 0.270.

(b) Average throat Mach number, $M_{t,av}$, 0.843.

Figure 36. - Comparison of experimental boundary-layer velocity profiles along cowl surface (station 19) with theoretical predictions for landing configuration (35 vanes; tapered thickness).

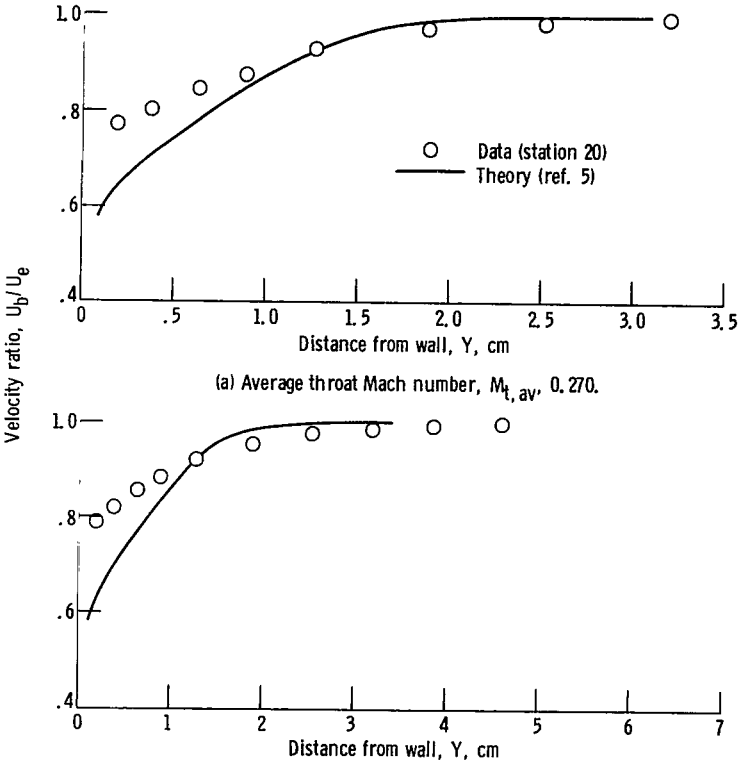

(a) Average throat Mach number, $M_{t,av}$, 0.270.

(b) Average throat Mach number, $M_{t,av}$, 0.843.

Figure 37. - Comparison of experimental boundary-layer velocity profiles along cowl surface (station 20) with theoretical predictions for landing configuration (35 vanes; tapered thickness).

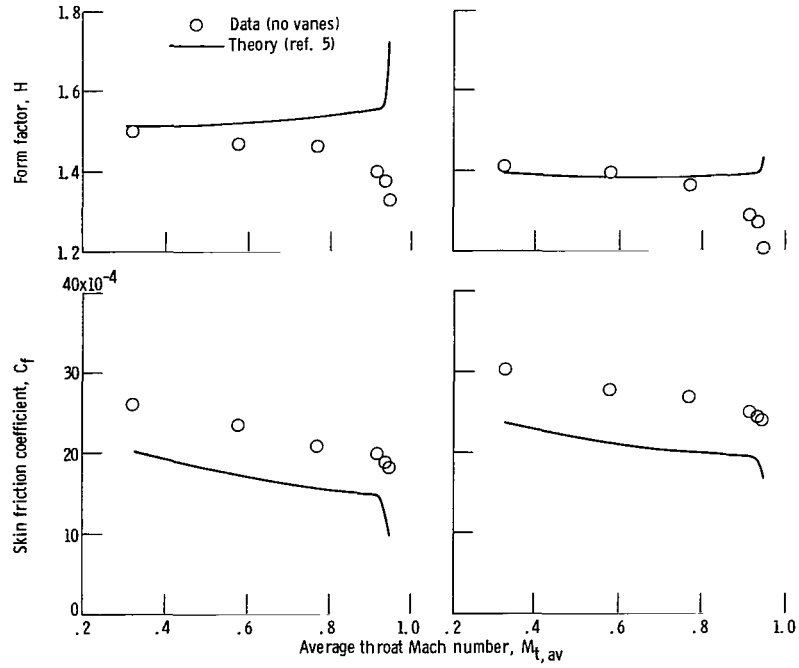

(a) Station 19. (b) Station 20.

Figure 38. - Variation of experimental skin friction coefficient and form factor with average throat Mach number and comparison with theoretical predictions for takeoff configurations (no vanes).

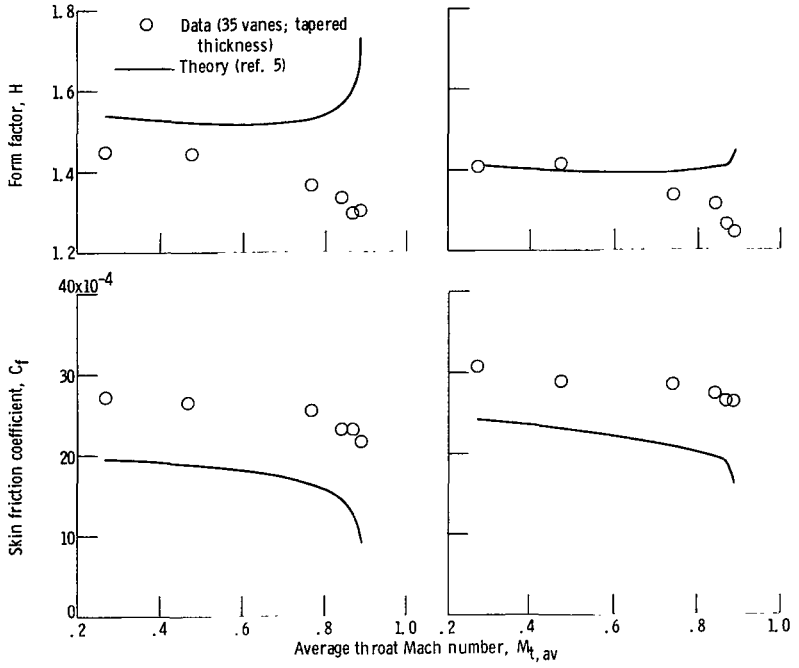

(a) Station 19. (b) Station 20.

Figure 39. - Variation of skin friction coefficient and form factor with average throat Mach number and comparison with theoretical predictions for landing configuration (35 vanes; tapered thickness).

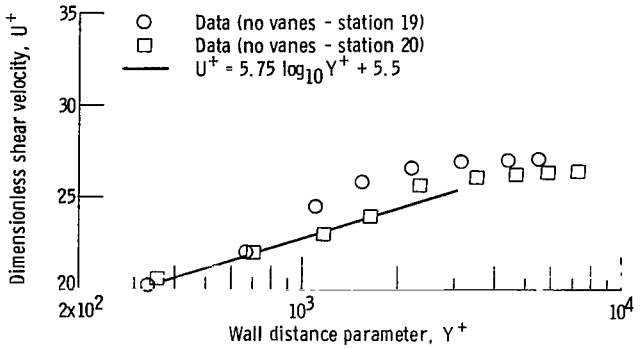

Figure 40. - Shear velocity distributions at stations 19 and 20 on cowl surface for takeoff configuration (no vanes) with average throat Mach number of 0.323.

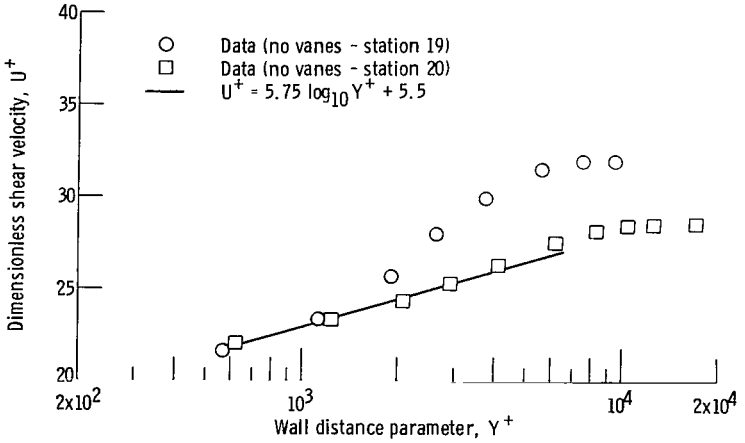

Figure 41. - Shear velocity distributions at stations 19 and 20 on cowl surface for takeoff configuration (no vanes) with average throat Mach number of 0.917.

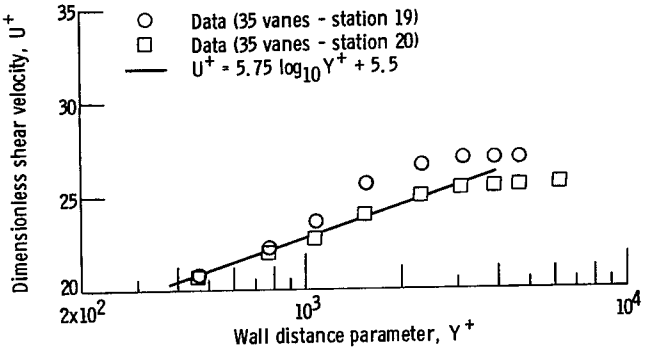

Figure 42. - Shear velocity distributions at stations 19 and 20 on cowl surface for landing configuration (35 vanes; tapered thickness) with an average throat Mach number of 0.270.

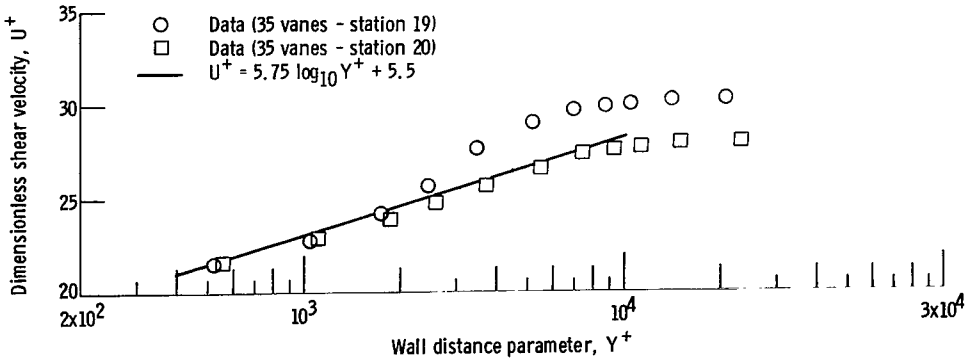

Figure 43. - Shear velocity distributions at stations 19 and 20 on cowl surface for landing configuration (35 vanes; tapered thickness) with average throat Mach number of 0.843.

846 001 C1 U A 761015 S00903DS
DEPT OF THE AIR FORCE
AF WEAPONS LABORATORY
ATTN: TECHNICAL LIBRARY (SUL)
KIRTLAND AFB NM 87117

"The aeronautical and space activities of the United States shall be conducted so as to contribute . . . to the expansion of human knowledge of phenomena in the atmosphere and space. The Administration shall provide for the widest practicable and appropriate dissemination of information concerning its activities and the results thereof."

—NATIONAL AERONAUTICS AND SPACE ACT OF 1958

NASA SCIENTIFIC AND TECHNICAL PUBLICATIONS

TECHNICAL REPORTS: Scientific and technical information considered important, complete, and a lasting contribution to existing knowledge.

TECHNICAL NOTES: Information less broad in scope but nevertheless of importance as a contribution to existing knowledge.

TECHNICAL MEMORANDUMS: Information receiving limited distribution because of preliminary data, security classification, or other reasons. Also includes conference proceedings with either limited or unlimited distribution.

CONTRACTOR REPORTS: Scientific and technical information generated under a NASA contract or grant and considered an important contribution to existing knowledge.

TECHNICAL TRANSLATIONS: Information published in a foreign language considered to merit NASA distribution in English.

SPECIAL PUBLICATIONS: Information derived from or of value to NASA activities. Publications include final reports of major projects, monographs, data compilations, handbooks, sourcebooks, and special bibliographies.

TECHNOLOGY UTILIZATION PUBLICATIONS: Information on technology used by NASA that may be of particular interest in commercial and other non-aerospace applications. Publications include Tech Briefs, Technology Utilization Reports and Technology Surveys.

Details on the availability of these publications may be obtained from:

SCIENTIFIC AND TECHNICAL INFORMATION OFFICE

NATIONAL AERONAUTICS AND SPACE ADMINISTRATION

Washington, D.C. 20546